Astronomy
&
Astrophysics

Perturbers: SPHERE detection limits to planetary-mass companions in protoplanetary disks

R. Asensio-Torres[1], Th. Henning[1], F. Cantalloube[1], P. Pinilla[1], D. Mesa[2], A. Garufi[3], S. Jorquera[4], R. Gratton[2], G. Chauvin[5,4], J. Szulágyi[6], R. van Boekel[1], R. Dong[7], G.-D. Marleau[8,9,1], M. Benisty[10,5], M. Villenave[5], C. Bergez-Casalou[1], C. Desgrange[1,11], M. Janson[12], M. Keppler[1], M. Langlois[13], F. Ménard[5], E. Rickman[14,15], T. Stolker[16], M. Feldt[1], T. Fusco[17,18], L. Gluck[5], A. Pavlov[1], and J. Ramos[1]

[1] Max-Planck-Institut für Astronomie (MPIA), Königstuhl 17, 69117 Heidelberg, Germany
  e-mail: henning@mpia.de
[2] INAF-Osservatorio Astronomico di Padova, Vicolo dell'Osservatorio 5, 35122 Padova, Italy
[3] INAF, Osservatorio Astrofisico di Arcetri, Largo E. Fermi 5, 50125 Firenze, Italy
[4] Unidad Mixta Internacional Franco-Chilena de Astronomía, CNRS/INSU UMI 3386 and Departamento de Astronomía, Universidad de Chile, Casilla 36-D, Santiago, Chile
[5] Université Grenoble Alpes, CNRS, IPAG, 38000, Grenoble, France
[6] ETH Zürich, Institute for Particle Physics and Astrophysics, Wolfgang-Pauli-Strasse 27, 8093 Zürich, Switzerland
[7] Department of Physics & Astronomy, University of Victoria, Victoria, BC V8P 1A1, Canada
[8] Institut für Astronomie und Astrophysik, Universität Tübingen, Auf der Morgenstelle 10, 72076 Tübingen, Germany
[9] Physikalisches Institut, Universität Bern, Gesellschaftsstr. 6, 3012 Bern, Switzerland
[10] Unidad Mixta Internacional Franco-Chilena de Astronomía (CNRS, UMI 3386), Departamento de Astronomía, Universidad de Chile, Camino El Observatorio 1515, Las Condes, Santiago, Chile
[11] Department of Physics, Ecole Normale Supérieure de Lyon, 69364, Lyon, France
[12] Department of Astronomy, Stockholm University, AlbaNova University Center, 106 91 Stockholm, Sweden
[13] Université de Lyon, CRAL/CNRS, CRAL, UMR 5574, CNRS, Saint-Genis-Laval, France
[14] Observatoire de Genève, Chemin Pegasi 51, 1290 Versoix, Switzerland
[15] European Space Agency (ESA), ESA Office, Space Telescope Science Institute, 3700 San Martin Dr, Baltimore, MD 21218, USA
[16] Leiden Observatory, Leiden University, Niels Bohrweg 2, 2333 CA Leiden, The Netherlands
[17] Aix Marseille Université, CNRS, CNES, LAM, Marseille, France
[18] DOTA, ONERA, Université Paris Saclay, 91123 Palaiseau, France

ABSTRACT

The detection of a wide range of substructures such as rings, cavities, and spirals has become a common outcome of high spatial resolution imaging of protoplanetary disks, both in the near-infrared scattered light and in the thermal millimetre continuum emission. The most frequent interpretation of their origin is the presence of planetary-mass companions perturbing the gas and dust distribution in the disk (perturbers), but so far the only bona fide planet detection has been the two giant planets carving the disk around PDS 70. Here, we present a sample of 15 protoplanetary disks showing substructures in SPHERE scattered-light images and a homogeneous derivation of planet detection limits in these systems. To obtain mass limits we rely on different post-formation luminosity models based on distinct formation conditions, which are critical in the first million years of evolution. We also estimate the mass of these perturbers through a Hill radius prescription and a comparison to ALMA data. Assuming that one single planet carves each substructure in scattered light, we find that more massive perturbers are needed to create gaps within cavities than rings, and that we might be close to a detection in the cavities of RX J1604.3-2130A, RX J1615.3-3255, Sz Cha, HD 135344B, and HD 34282. We reach typical mass limits in these cavities of 3–10 $M_{\rm Jup}$. For planets in the gaps between rings, we find that the detection limits of SPHERE high-contrast imaging are about an order of magnitude away in mass, and that the gaps of PDS 66 and HD 97048 seem to be the most promising structures for planet searches. The proposed presence of massive planets causing spiral features in HD 135344B and HD 36112 are also within SPHERE's reach assuming hot-start models. These results suggest that the current detection limits are able to detect hot-start planets in cavities, under the assumption that they are formed by a single perturber located at the centre of the cavity. More realistic planet mass constraints would help to clarify whether this is actually the case, which might indicate that perturbers are not the only way of creating substructures.

Key words. protoplanetary disks – planet-disk interactions – planets and satellites: detection – techniques: high angular resolution – techniques: image processing

1. Introduction

Protoplanetary disks (PPDs) are the by-product of the star formation process, and the place where giant planets form before all the gas is accreted onto the star or dispersed over a period of ~3–10 Myr (Fedele et al. 2010). In the last few years, high-resolution observations have opened a new era in our understanding of the gas and dust around young stars. These observations show a plethora of complex substructures in PPDs that are remarkably common when imaged with sufficient angular

resolution, including gaps, cavities, rings, vortices, asymmetries, and spiral arms (e.g., van Boekel et al. 2017; Avenhaus et al. 2018; Andrews et al. 2018; Long et al. 2019; Garufi et al. 2020).

The origin of these morphologies remains unclear, and different mechanisms have been proposed to explain them (e.g., Flock et al. 2015; Okuzumi et al. 2016; Takahashi & Inutsuka 2016; Cieza et al. 2016; Gonzalez et al. 2017; Dullemond & Penzlin 2018; Riols et al. 2020). A common interpretation is to describe them as signposts of planetary-mass companions interacting with the disk, which requires a formation of the giant planets and their location within the gaps in less than a few million years. In this scenario the massive planet creates a pressure bump in the gas that stops the radial drift of the dust, which gets trapped in the pressure maxima and creates a ring-like structure. In general, millimetre-sized (mm-sized) dust is affected by the drag with the gas and it is easily trapped in pressure bumps (Drążkowska et al. 2016; Taki et al. 2016). However, micrometre-sized (μm-sized) dust is coupled to the gas, following its distribution and possibly populates the gap. As a result, spatial segregation is expected in the distribution of small and large dust particles (Rice et al. 2006; de Juan Ovelar et al. 2013; Pinilla et al. 2015; Hendler et al. 2018). The exact morphology and structure of these regions will eventually depend on planet mass and PPD properties, such as viscosity and temperature (e.g., Whipple 1972; Pinilla et al. 2012).

To understand how these structures are formed and to shed light on the planet formation mechanism, SPHERE high-resolution scattered-light observations probe the surface layers of the optically thick dust using the polarised differential imaging technique (PDI; de Boer et al. 2020; van Holstein et al. 2020). This mode detects the polarised light scattered off μm-sized grains, and is thus an effective way of removing the stellar halo without altering the underlying disk morphology with post-processing techniques. To date, there are ~90 disks imaged in this mode; the images were obtained via individual observations of large disks around intermediate-mass stars (e.g. Benisty et al. 2015; Ginski et al. 2016; Stolker et al. 2016; Pohl et al. 2017), and also via surveys designed to mitigate observational biases, such as Disks ARound T Tauri Stars with SPHERE (DARTTS-S; Avenhaus et al. 2018). These results show a ubiquity of substructures in scattered light in IR bright disks, unless the disks are small or too faint.

The indirect detection of protoplanets creating these observed PPD substructures is particularly hindered by the presence of circumstellar material, while stellar activity also limits the performance of radial velocity surveys. Currently, direct imaging is the best technique for simultaneously detecting and characterising the planet and the disk morphology, although the companion luminosity might also be affected by extinction due to the surrounding disk material (Szulágyi et al. 2018, 2019; Szulágyi & Garufi 2021; Sanchis et al. 2020). So far, with the exception of the two planets around PDS 70 (Keppler et al. 2018; Müller et al. 2018; Haffert et al. 2019; Mesa et al. 2019), only unconfirmed planetary-mass candidates have been found with direct imaging in PPDs. A few kinematic detections of embedded protoplanets have been proposed (Pinte et al. 2018, 2019; Teague et al. 2018), but there has not been a final confirmation of these objects.

Detection limits to low-mass companions via total intensity high-contrast imaging data are available for only a handful of targets that show hints of substructures. These data, however, were analysed with different algorithms that remove the stellar halo, using different mass-luminosity relationships, and sometimes outdated and heterogeneous stellar parameters.

In this paper, we present a homogeneous study to determine planet detection limits within the substructures of a sample of PPDs observed in μm-sized dust with SPHERE. Our goal is to perform a systematic analysis to planet sensitivities in these systems, and to understand how far we are from detecting perturbers with direct imaging. In Sect. 2 we motivate the PPD sample and present the high-contrast imaging reduction of the data. In Sect. 3 we convert the obtained detection limits to mass sensitivities, and assess the effect of different formation luminosities on the detectability of low-mass companions. In Sect. 4 we estimate the mass and location of the potential companions carving these substructures, and compare them to the SPHERE detection limits. Finally, in Sect. 5 we discuss the results and caveats of this paper, and in Sect. 6 we present the conclusions.

2. Sample selection and data reduction

We collected PPD systems observed with SPHERE that comply with the following criteria: (1) the PPD shows rings, cavities, or spirals in SPHERE/PDI observations; (2) the host star is single or has no stellar companions closer than 3″; (3) the PPD has an inclination below ~60 deg; and (4) the PPD has been observed in coronagraphic angular differential imaging mode (ADI, Marois et al. 2006) with SPHERE, suitable for the detection of low-mass companions.

The resulting list of targets includes disks that have substructures observed in the small dust component, and allows us to obtain sensitivities to planets that are not critically affected by projection effects and extinction towards the line of sight (e.g., Szulágyi & Garufi 2021). Moreover, our selection removes close binaries to optimise that the physical and morphological properties of the PPDs are not influenced by the presence of a stellar companion; this allows us to attribute the substructures to intrinsic physical processes related to the disk or host star (e.g., Durisen et al. 2007), or otherwise to the presence of planetary-mass objects.

The target selection was mostly based on the compilation by Garufi et al. (2018) and the latest results of the DARTTS-S survey (Avenhaus et al. 2018; Garufi et al. 2020), followed by a cross-match with the ESO archive of ADI data. The final sample is comprised of 15 PPDs, whose substructures are characterised based on their visual appearance in the PDI images. Garufi et al. (2018) classified them as Spirals, Ring, Rim, Giant, Faint, Small, and Inclined. This classification is subjective and can be affected by projection effects and the observing conditions of the different datasets; this implies that some PPDs will have some overlap, for instance in the form of rims and/or rings (e.g. PDS 66) or giants with spirals (e.g. HD 100546). In this section we further simplify the classification and assign one class to each PPD depending on which feature is most prominent; Spiral when spiral arms in the μm-sized dust are seen, Rings when the PPD shows signs of a series of resolved rings with gaps in between those, and Rim when there is a detection of a large central cavity with a clear bright rim (typically known as transition disks). Some systems reveal different substructures when observed with ALMA in the gas or mm-sized dust (e.g., Teague et al. 2019), but we do not consider those images for the classification. HD 100546 and HD 34282 are complicated systems where arcs, spirals and cavities are present. Here we put them in the Spiral group, but the presence of rims or rings in these systems will also be taken into account (see Appendix A). For instance, HD 34282 hosts an inner cavity with a rim-like structure at ~88 au, and a potential single-armed spiral feature farther out better observed after deprojection (de Boer et al. 2021). These individual

Table 1. Stellar parameters of the targets.

Target	RA (J2000) (h:m:s)	Dec (J2000) (deg:m:s)	SpT	V (mag)	d (pc)	Teff (K)	L_* (L_{Sun})	A_V (mag)	M_* (M_{Sun})	Age (Myr)
LkCa 15	04:39:17.79	+22:21:03.38	K5	12.0	157.2 ± 0.6	4800	1.11 ± 0.04	0.6	1.2 ± 0.1	$6.3^{+0.7}_{-1.9}$
HD 34282	05:16:00.47	−09:48:35.39	B9.5	9.8	318.6 ± 2.2	9400	19.0 ± 1.8	0.6	1.9 ± 0.1	$8.9^{+0.7}_{-1.9}$
HD 36112	05:30:27.52	+25:19:57.08	A8V	8.3	155.9 ± 0.8	8200	11.8 ± 0.5	0.2	1.8 ± 0.1	$8.9^{+2.1}_{-1.0}$
CQ Tau	05:35:58.46	+24:44:54.08	F5IV	10.0	149.4 ± 1.3	6800	7.3 ± 0.6	0.4	1.4 ± 0.1	$9.9^{+2.1}_{-2.9}$
Sz Cha	10:58:16.74	−77:17:17.18	K0	12.7	190.2 ± 0.9	4900	2.6 ± 0.2	1.5	1.5 ± 0.2	$1.9^{+0.9}_{-0.7}$
TW Hya	11:01:51.90	−34:42:17.03	K6V	10.5	60.14 ± 0.05	4000	0.33 ± 0.02	0.0	0.8 ± 0.1	$6.3^{+3.7}_{-1.9}$
HD 97048	11:08:03.31	−77:39:17.49	A0V	9.0	184.4 ± 0.8	10 400	44.2 ± 5.7	1.1	2.4 ± 0.2	$3.9^{+1.7}_{-0.4}$
HD 100546	11:33:25.44	−70:11:41.23	A0V	6.3	108.1 ± 0.4	9800	31.6 ± 0.7	0.1	2.2 ± 0.2	$5.0^{+1.3}_{-0.6}$
PDS 66	13:22:07.54	−69:38:12.21	K1V	10.4	97.9 ± 0.1	4600	1.26 ± 0.04	0.8	1.2 ± 0.2	$3.1^{+0.8}_{-0.9}$
PDS 70	14:08:10.15	−41:23:52.57	K7IV	12.2	112.4 ± 0.2	4000	0.31 ± 0.02	0.0	0.8 ± 0.1	$7.9^{+3.1}_{-2.9}$
HD 135344B	15:15:48.44	−37:09:16.02	F8V	8.7	135.0 ± 0.4	6400	6.9 ± 0.4	0.4	1.5 ± 0.1	$8.9^{+2.1}_{-1.1}$
HD 139614	15:40:46.38	−42:29:53.53	A9V	8.2	133.6 ± 0.5	7800	7.0 ± 1.6	0.0	1.6 ± 0.1	$12.2^{+4.1}_{-1.1}$
RX J1604.3-2130A	16:04:21.65	−21:30:28.54	K2	12.3	145.3 ± 0.6	4600	0.60 ± 0.03	1.1	1.0 ± 0.1	$11.1^{+3.3}_{-3.1}$
RX J1615.3-3255	16:15:20.23	−32:55:05.09	K5	12.0	155.6 ± 0.6	4000	0.90 ± 0.02	0.6	0.6 ± 0.1	$1.0^{+0.4}_{-0.2}$
HD 169142	18:24:29.77	−29:46:49.32	F1V	8.2	114.0 ± 0.8	7400	5.6 ± 1.2	0.0	1.5 ± 0.2	$12.3^{+6.4}_{-1.2}$

Notes. Stellar parameters of the PPD hosts considered in this work. References for the stellar temperature and optical extinction can be found in Table F.1 of Garufi et al. (2018). Mass, luminosity and age have been derived here using *Gaia* EDR3 parallaxes (Gaia Collaboration 2021).

substructures within a given PPD (not the global classification made in this section) will be taken into account separately to derive potential planet masses and locations in Sect. 4.

2.1. Stellar parameters

In Table 1, we show the derived parameters for the stellar hosts present in our sample. We followed the method outlined in Garufi et al. (2018), but in this case we obtained updated values using the new *Gaia* Early Data Release 3 parallaxes (*Gaia* ED3, Gaia Collaboration 2016, 2021). We built the stellar SEDs using *VizieR* and fit the wavelength range 0.4 μm–1.3 mm to the PHOENIX photospheric models (Hauschildt et al. 1999), which allowed us to calculate the stellar luminosity using literature extinction A_V and effective temperature T_{eff}. In the left panel of Fig. 1 we show a Hertzsprung–Russell diagram of the sample, where we estimate each individual mass and age using the MIST pre-main-sequence (PMS) tracks (Choi et al. 2016). These isochrones are consistent with other PMS tracks such as Parsec (Bressan et al. 2012), Baraffe (Baraffe et al. 2015) and Dartmouth (Dotter et al. 2008). To calculate the uncertainties on the age and mass, the error bars on the luminosity (in turn derived from a 20% uncertainty on the optical extinction) and on T_{eff} (± 200 K) was propagated through the tracks. The right panel shows the location of the targets in the stellar mass-distance space. Distances to the targets range between 60 and 300 pc, but most of them lie around 150 pc, as members of star-forming regions such as Sco-Cen and Taurus. Spirals tend to appear in disks around massive stars, while objects classified as Rim, with prominent cavities, are only resolved in the scattered light in <1.5 M_{Sun} stellar systems (although some of the most massive objects classified as Spiral also count with resolved cavities; see Appendix A).

We note here that the derived isochronal parameters for young PMS stars carry a moderate uncertainty. Stellar age is the most critical parameter to estimate reliable sensitivities to planet mass; deviations in L/T_{eff} values, the use of different evolutionary tracks, the effect of magnetic fields, and the initial position of the star at $t = 0$ can all contribute to dubious estimations of individual ages (e.g., Asensio-Torres et al. 2019). Our approach allows us to obtain a homogeneous and consistent classification of the different PPDs, while the adopted ages (Table 1) also tend to agree, within error bars, with other individual studies. For instance, PDS 70 is found to have an age of 5.4 Myr (Müller et al. 2018), and TW Hya is most consistent with 8 Myr (Sokal et al. 2018). HD 139614 has an age of 10.75 ± 0.77 Myr, recently derived via astereoseismology (Murphy et al. 2021), in close agreement with our values. For HD 169142, an estimation of 6^{+6}_{-3} Myr was found for the M-type wide binary companion 2M1824 (Grady et al. 2007), for which only the upper uncertainty value is consistent with our estimation, although isochronal ages for low-mass stars seem to be underestimated by a factor of ~2 (Asensio-Torres et al. 2019).

2.2. Reduction of the pupil-tracking data

For all the objects in the target list of Table 1, we performed high-contrast imaging ADI reductions to obtain detection limits to the presence of perturbers creating the substructures in the small dust distribution. Table 2 shows the corresponding pupil-tracking epochs. When more than one ADI observation of the same system was available, we analysed the epoch that provided a better contrast based on published results, collected sky rotation and weather conditions (see Table 3). The ADI observing modes are split about equally between IRDIFS and IRDIFS-EXT; IRDIFS was the preferred mode by the SpHere INfrared Exoplanets survey (SHINE; e.g. Chauvin et al. 2017), which mainly targeted nearby stars 10–200 Myr in age. This mode results in dual-band imaging in the H band with the infrared
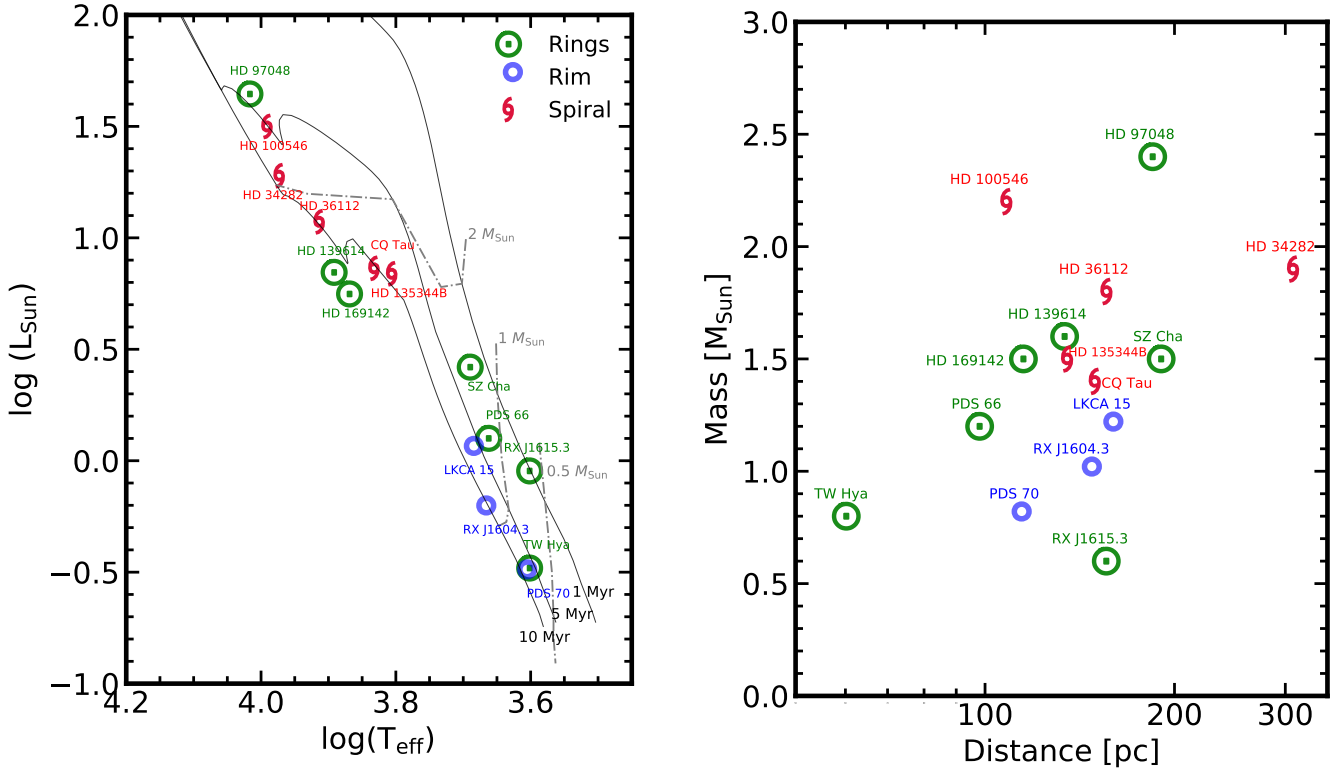
Fig. 1. *Left*: Hertzsprung–Russell diagram of the PPD hosts in our sample. They are classified into Rings, Rim, or Spiral based on their main detected substructures; the MIST tracks for young PMS stars are overplotted (Choi et al. 2016). The resulting stellar parameters are shown in Table 1 and have been derived as explained in Sect. 2.1. *Right*: mass–distance diagram of the same population.

Table 2. Perturber ADI epochs.

Target	Date (UT)	Programme ID	t_{int} (min)	Sky rot (deg)	Inc (deg)	PA (deg)	Mode	Global substructure
LkCa 15	2015-11-29	096.C-0241(B)	84.3	26.4	50	60	IRDIFS_EXT	Rim
HD 34282	2015-10-26	096.C-0241(A)	67.2	53.5	56	119	IRDIFS	Spiral
HD 36112	2018-12-17	1100.C-0481(K)	102.4	29.1	21	62	IRDIFS	Spiral
CQ Tau	2016-12-21	298.C-5014(A)	126.7	44.4	35	55	IRDIFS_EXT	Spiral
Sz Cha	2017-02-10	198.C-0209(E)	102.4	34.3	48.9	158.3	IRDIFS	Ring
TW Hya	2015-02-04	095.C-0298(H)	67.2	76.7	7	320	IRDIFS	Rim
HD 97048	2016-03-28	096.C-0241(E)	84.3	24.5	39.9	2.8	IRDIFS	Ring
HD 100546	2015-05-29	095.C-0298(B)	102.1	34.3	42.5	139.1	IRDIFS	Spiral
PDS 66	2017-02-11	198.C-0209(E)	116.3	38.5	30.1	189.2	IRDIFS	Ring
PDS 70	2018-02-25	1100.C-0481(D)	142.4	95.7	49.7	158.6	IRDIFS_EXT	Rim
HD 135344B	2015-05-15	095.C-0298(A)	67.2	63.6	11	62	IRDIFS_EXT	Spiral
HD 139614	2017-06-12	198.C-0209(H)	100.8	69.6	17.6	276.5	IRDIFS	Ring
RX J1604.3-2130A	2015-06-10	095.C-0673(A)	93.3	142.8	6	80	IRDIFS_EXT	Rim
RX J1615.3-3255	2015-05-15	095.C-0298(A)	67.2	74.3	47	146	IRDIFS	Ring
HD 169142	2019-05-18	1100.C-0481(N)	76.8	118.4	13	5	IRDIFS_EXT	Ring

Notes. ADI observations of the target list in Table 1. The IRDIS side of the observations was obtained in dual-band mode (H2-H3 and K1–K2 for IRDIFS and IRDIFS-EXT, respectively), except for CQ Tau, for which the full K_s band was used. References for the inclination (Inc) and position angle (PA) of the disks can be found in Appendix A.

dual-band imager and spectrograph (IRDIS; Dohlen et al. 2008), and *YJ* spectrophotometry with the near-infrared integral field spectrograph (IFS; Claudi et al. 2008) in the Y–J range with a field of view (FoV) of $1.7'' \times 1.7''$. With the inclusion of younger stars located beyond 100 pc in the survey (particularly from Sco-Cen) or dedicated follow-up of PPDs, the IRDIFS-EXT mode was used, which extends the dual-band imaging to the *K* band and the IFS spectrophotometry to the *H* band, as

this mode is more adapted for the detection of young red L-type planets.

The reduction and analysis were conducted homogeneously for the entire dataset. For the IRDIS side we first used the vlt-sphere repository (Vigan 2020)[1], which is a python-based pipeline to pre-reduce SPHERE data (Beuzit et al. 2019). We

---

[1] https://github.com/avigan/SPHERE

Table 3. Weather conditions of the ADI epochs.

Target	Wind speed (m s^{-1})	τ_0 (ms)	Seeing ($''$)
LkCa 15	1.0	19.5	1.53
HD 34282	1.8	1.3	1.18
HD 36112	4.1	6.9	1.02
CQ Tau	5.0	8.3	0.69
Sz Cha	4.9	3.7	0.69
TW Hya	4.5	11.5	0.58
HD 97048	8.5	3.6	0.95
HD 100546	8.2	1.7	0.81
PDS 66	11.4	2.8	0.99
PDS 70	2.9	7.0	0.42
HD 135344B	6.5	8.5	0.50
HD 139614	13.9	1.5	1.81
RX J1604.3-2130A	11.0	2.0	1.40
RX J1615.3-3255	6.9	6.7	0.64
HD 169142	12.6	4.1	0.43

Notes. Median wind speed, turbulence coherence time and seeing during the ADI observations of Table 2. Low wind effects are usually avoided with a wind speed >3 m s^{-1}, and a $\tau_0 > 3$ ms effectively eradicates the wind-driven halo in SPHERE observations.

sorted out the files and performed static calibrations, such as flat-field reduction, dark and sky subtraction, and bad pixel correction. This was followed by star registration, for which we used the waffle pattern to find the location of the host star behind the coronagraphic mask, and flux calibration to get the difference in flux between the unsaturated star and the science frames. After this pre-reduction step we obtained a cube of centred saturated frames, collapsed unsaturated stellar frames for flux calibration, a sky rotation file and the wavelength in which the observations were carried out. To treat the quasi-static speckle noise affecting high-contrast imaging observations, further PSF-removal was conducted with the ANgular DiffeRential OptiMal Exoplanet Detection Algorithm (ANDROMEDA; Cantalloube et al. 2015). This algorithm is based on the maximum likelihood estimation. It first attenuates extended structures by applying a high-pass Fourier filtering that removes 25% of the lowest frequencies (with an energy loss of ~18%; see Fig. 1 in Cantalloube et al. 2015). Subsequently, ANDROMEDA performs a model cross-correlation of the signature that a point source leaves after two frames at different rotation angles are subtracted. This processing is thus sensitive to the presence of point sources in the field of view. Before feeding the vlt-sphere output to ANDROMEDA, we performed a frame selection to remove those that deviate more than n standard deviations of the mean of the 3D cube in a 20 px radius centred on the star. The process is repeated for $n = 1, 2, 3 \ldots$ until the rejection fraction is lower than 20%. Finally, ANDROMEDA provides two 2D maps: (i) the estimated contrast that a point source would have at every location in the image, and (ii) the corresponding uncertainty on this estimated contrast. The limiting contrast is therefore given by the uncertainty map, previously normalised empirically to account for the non-Gaussian residual noise at small separation (Cantalloube et al. 2015). This map can be used to derive a 1D 5σ projected detection limit by taking its azimuthal median.

The IFS data was pre-reduced via the SPHERE Data Center (Delorme et al. 2017), and the resulting cubes went through the SpeCal software (Galicher et al. 2018), which further removes

the stellar halo by applying an ADI-based method. We selected an Angular and Spectral Differential Imaging (ASDI) reduction following the principal component analysis approach in Mesa et al. (2015) for the spatial and spectral channels. This method is aggressive in terms of speckle subtraction and seems to reach better contrasts than IRDIS-ADI within the IFS FoV (Langlois et al. 2021). Moreover, 1D IFS-ASDI projected contrast curves were computed as the azimuthal standard deviation of the noise residuals, corrected for self-subtraction via fake planet injections. To obtain 2D IFS-ASDI limiting magnitude maps that account azimuthally for the presence of disk residuals, we evaluated, around each pixel, the standard deviation within a ring of inner and outer radius of 0.7 and 2.5 FWHM, respectively.

3. Detection limits

In Fig. 2, we show the projected 1D contrast limits achieved by ANDROMEDA/IRDIS and SpeCal-ASDI/IFS for the entire PPD sample. In general, ANDROMEDA/IRDIS achieves magnitude differences of ~11–14 mag at 0.5$''$ in the contrast-limited regime, and down to 16 mag at larger separations limited by background sensitivity. With the use of ASDI, IFS contrasts seem to improve the IRDIS limits at close separations, within ≲0.4$''$. In addition to the presence of disk residuals, factors contributing to the final detection limits include variations in Strehl ratio, weather conditions, collected sky rotations, and magnitudes of the host stars.

To convert these contrasts to detectable companion masses, a post-formation luminosity of the perturber needs to be assumed. This is known as the initial luminosity with respect to the cooling phase, and is set by the radiative transfer and thermodynamics during the accretion phase (e.g., Mordasini et al. 2017; Szulágyi & Mordasini 2017; Marleau et al. 2019a). These differences can lead to divergences between the hot (more luminous) and cold (fainter) starts of about three orders of magnitude in luminosity during the first few million years (e.g., Marley et al. 2007; Spiegel & Burrows 2012). Although it is likely that a smooth range in planet formation luminosities between the extreme hot and cold models exists, the coldest starts do not seem to be a valid representation of the physical conditions of the current population of imaged planets; for instance, dynamical masses of the two planets around β Pic seem to fall close to the predictions of a hot start, either formed through disk instability or a hot core accretion process (Brandt et al. 2021; Nowak et al. 2020). Likewise, cold starts are unable to reproduce the dynamical masses of the four giant planets in the HR 8799 system (Wang et al. 2018). Although these results could be affected by an observational bias, where we simply have not yet detected cold-start planets because they are fainter (see Sect. 5.1), theoretical studies of the accretion shock also favour hotter start models (Marleau et al. 2019b).

Here we rely on the AMES-DUSTY atmospheric models (Chabrier et al. 2000) to reproduce the hottest, most luminous outcome of planet formation, usually associated with disk instability. This model includes dust absorption and scattering, since young planets seem to have condensates in their atmospheres (e.g., Müller et al. 2018). AMES-DUSTY has been widely used by the community, and starts with a completely formed planet at arbitrary initial entropy for a given mass.

We also use the Bern EXoplanet cooling curves (BEX), which are based on the population synthesis models by Mordasini et al. (2017). They provide luminosities of young giant planets formed through the core accretion paradigm. Depending on whether the accretion shock luminosity is radiated away or
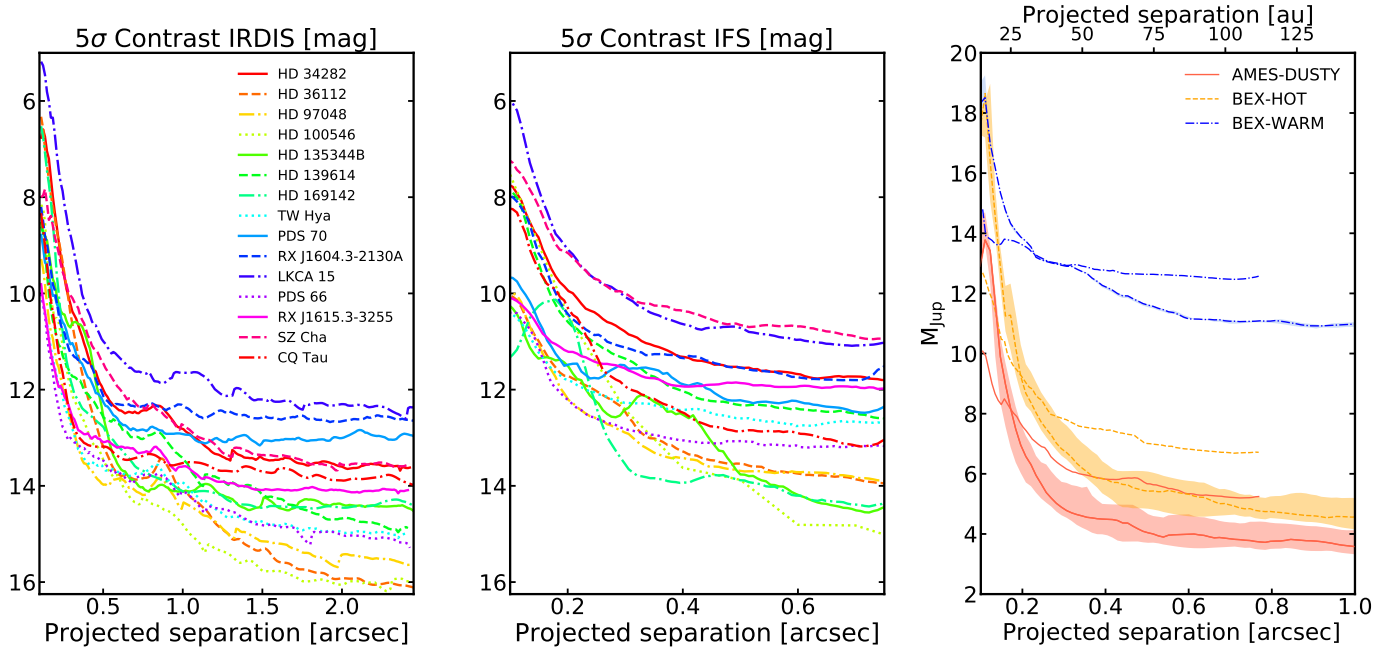
Fig. 2. *Left*: SPHERE 1D projected contrast curves for ANDROMEDA/IRDIS data in the $H2$, $K1$, or K_s filter, depending on the observing mode given in Table 2. The results are shown down to the edge of the coronagraph (∼100 mas). *Centre*: corresponding ASDI/IFS magnitude limits for the inner regions. *Right*: median mass detection limits assuming the initial luminosities given by the AMES-DUSTY, BEX-HOT, and BEX-WARM models. To convert the semi-major axis to au, a median distance was adopted in our sample of ∼145 pc. Thick curves correspond to the ANDROMEDA/IRDIS performance, while the shaded areas show the median sensitivities for the upper and lower limits on the age of the companions. ASDI/IFS mass limits are shown in the same curve style up to ∼0.8″. Individual deprojected detection limits are given in Appendix B.

deposited into the planet, the initial luminosities of the newborn planets are classified in diminishing order of brightness from hottest to coldest. These are then expanded into evolutionary tracks at constant mass, reproducing the cooling under different atmospheric conditions (Marleau et al. 2019a). We make use of the BEX-COND tracks, where the initial planet luminosities are coupled to the boundary conditions given by the condensate-free AMES-COND atmospheric models (Allard et al. 2001), and use these resulting BEX-COND gravities and temperatures as a function of time to calculate the magnitudes via DUSTY. We adopt the hot- and warm-start initial conditions from BEX-COND, which we call BEX-HOT and BEX-WARM. These two relations correspond to a fit extension of the cold nominal (BEX-HOT) and cold classical (BEX-WARM) population in Marleau et al. (2019a); see Eq. (1) in Vigan et al. (2021).

In the right panel of Fig. 2, we see the effect of these different post-formation luminosities on the median projected sensitivity to planet masses around a stellar host located at the typical distance of our sample (145 pc). Down to ∼15 au (0.1″), assuming that the AMES-DUSTY models are valid, the SPHERE observations would be sensitive to planets below 10 M_{Jup}, and down to 4 M_{Jup} at >0.5″. This is different by a factor ∼×1.5 if the BEX-HOT start models are considered, and planets below 11 M_{Jup} would not be detectable if the cold BEX-WARM models are a good representation of planet formation.

There are, however, a few caveats in the use of evolutionary models. If the perturber is formed via core accretion, there will be a delay time with respect to the formation of its host star (e.g., Fortney et al. 2005; Bonnefoy et al. 2014). For gas giants the delay cannot be longer than the typical PPD lifetime of ∼3 Myr (e.g. Ribas et al. 2015); most giant planets around an A-type star will have acquired their final mass after 2 Myr (Williams & Cieza 2011; Marleau et al. 2019a). Moreover, if the planet is still forming, its intrinsic luminosity could be augmented by

accretion onto the planet surface and/or by shock and thermal emission from a potential circumplanetary disk (CPD; Szulágyi et al. 2014; Zhu 2015; Szulágyi & Mordasini 2017; Aoyama et al. 2018, 2021; Aoyama & Ikoma 2019), while at the same time also reddened by the presence of material in the circumplanetary environment (Szulágyi et al. 2018, 2019; Szulágyi & Ercolano 2020). In the cases where formation is ongoing these evolutionary models of post-formation luminosities are probably not a very solid representation of the physical parameters of the perturbers. However, without comprehensive spectroscopic analysis it is extremely difficult to derive the mass of a forming protoplanet from the expected magnitudes, as the contribution of accretion can be very important, creating a spread in luminosity of up to ∼2 dex for a given planet mass (see Fig. 2 in Mordasini et al. 2017). Here we suppose that the perturber starts its post-formation cooling at the same time as the star reaches its PMS phase, and assume that any potential time delay would be included within the estimated error bars on the age of the host star. Extinction effects are discussed in Sect. 5.2.

Finally, we convert the projected 2D limiting contrasts to mass limits for each pixel in the image. These are then used to obtain a detection probability map for each target (included in Appendix C) via the Multi-purpose Exoplanet Simulation System (MESS, Bonavita et al. 2012) and to obtain 1D deprojected mass sensitivities. For the latter, we deprojected the 2D maps by inclination and position angle to be in the disk plane (see Fig. 3 for an ANDROMEDA/IRDIS example, and 4 for the ASDI/IFS mode), and at each radial separation we took the median of the limiting mass values to construct 1D sensitivities, which are shown for each individual system in Appendix B. We also overplot the location of the substructures seen in scattered light and in the millimetre continuum as explained in Appendix A. In the following section we use this method to constrain the detectability of the perturbers that may be creating the PPD substructures.
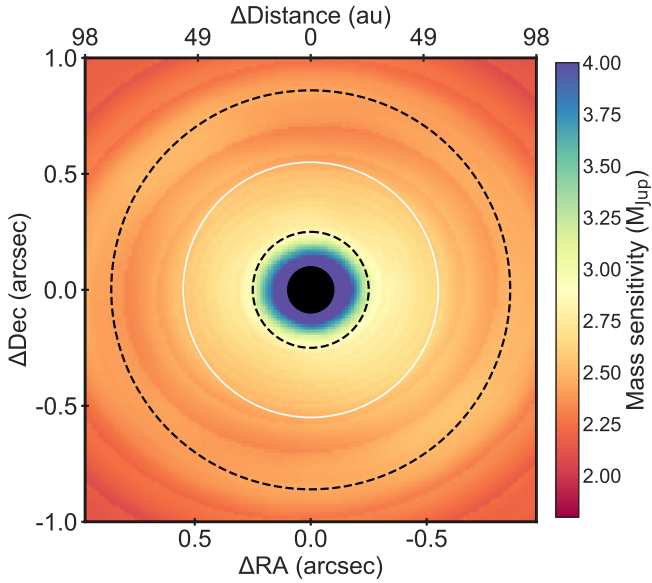
Fig. 3. 5σ mass sensitivity to companions in the PDS 66 system and the IRDIS *H*2 filter. The removal of the stellar halo was performed with ANDROMEDA, and AMES-DUSTY initial conditions are assumed for the perturber's luminosity. The black dashed circumferences show the outer radius of the bright compact region at 25 au and the location of the outer ring at 85 au, respectively, as seen in scattered light by Avenhaus et al. (2018). The white thick circumference shows the proposed location of a perturber, at 55 au, creating the ring-like substructure, which coincidentally corresponds to a further depleted region in the scattered-light data. The black circle shows the location of the star and has a radius of 0.1 ″. The 2D map has been deprojected based on the disk parameters of Table 1.
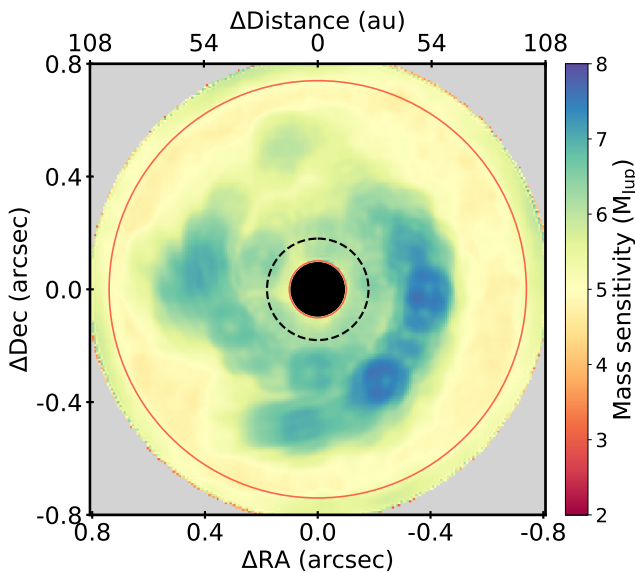
Fig. 4. 5σ mass sensitivity to companions in the HD 135344B system achieved by the ASDI/IFS reduction. As in Fig. 3, AMES-DUSTY initial conditions are assumed for the perturber's luminosity, and the 2D map was deprojected based on the disk parameters listed in Table 1. Disk residuals caused by the spiral pattern are clearly seen. The black dashed circumference shows the location of the cavity in scattered light as observed by SPHERE/PDI (Stolker et al. 2016). The inner red thick circumference shows the proposed location of a perturber in the middle of the cavity, very close to the coronagraphic mask, and the outer circumference represents the proposed location of a 5–10 $M_{\rm Jup}$ companion creating the spirals (Dong & Fung 2017a).

4. Population of perturbers in SPHERE PPDs

To approximate the mass and location of the perturbers causing the substructures in the PPDs in our sample, we first rely on the simulated results in the literature where gap morphology in the μm-sized dust is taken into account (Pohl et al. 2017; Dong & Fung 2017b; van Boekel et al. 2017), together with the simulated planets that may reproduce the spirals in scattered light (Dong & Fung 2017a; Baruteau et al. 2019). However, these derivations make up only a subset of the substructures seen in our target list. Given the intricate disk–planet interaction and the large numbers of gap structures we are dealing with, in addition to the simulated perturbers obtained from the literature we also consider two different ways of estimating their masses: (1) gap width proportional to the planet Hill radius and (2) difference in cavity size in near-infrared scattered-light images and ALMA millimetre continuum.

4.1. Gap opening mass from Hill radii

The gap width that a planet carves in the disk can be approximated by a proportionality factor applied to its Hill sphere of influence, defined as $R_{\rm Hill} = R_{\rm p} \, (M_{\rm p}/3M_\star)^{1/3}$. A simple estimation that can relate the observed width in scattered light to the perturber's mass is given by

$$R_{\rm PDI,peak} - R_{\rm PDI,gap} = k \, R_{\rm Hill}, \tag{1}$$

where the width is defined as the distance between the gap minimum $R_{\rm PDI,gap}$ and the peak of the ring $R_{\rm PDI,peak}$ seen in PDI, and k is a scaling factor. This formulation is similar to the latest estimations of gap-carving planet masses in the millimetre continuum (e.g. Lodato et al. 2019), which are in agreement with the individually modelled DSHARP planet population and the broader collection from Bae et al. (2018).

To estimate the scaling factor in the μm-sized dust, we consider the gap located at ∼127 au in the PPD around HD 97048. The edges of this gap are well resolved in SPHERE/PDI and total intensity, and the surface brightness of the bottom is detected at 5σ background sensitivity (Ginski et al. 2016). First, we apply the analytical gap-opening criterion from Crida et al. (2006), which does not take into account gap morphology nor dust dynamics and evolution. This solution gives the minimum planet mass that clears 90% of the gas disk when the following criterion is met:

$$\frac{3}{4}\frac{H}{R_{\rm Hill}} + \frac{50}{qRe} \lesssim 1. \tag{2}$$

Here H is the local scale height and Re the Reynolds number defined as $r_{\rm p}2\Omega_{\rm p}/\nu$, with $r_{\rm p}$ being the radius of the planet orbit, $\Omega_{\rm p}$ the angular velocity and ν the viscosity $\nu = \alpha c_{\rm s}^2/\Omega_{\rm p}$. The shaded area of Fig. 5 shows the allowed mass values according to this approach for $\alpha = 10^{-3}$ and assuming $H/r_{\rm p} = 0.056$, which is the same value found by Dong & Fung (2017b) at the gap location through Eq. (4) (see below). A perturber with a mass $\geq 1.3 \, M_{\rm Jup}$ is necessary to create a well-depleted gap in the gas.

To take into consideration the morphological features that a planet causes in the disk, hydrodynamical simulations have investigated the gap parameters that a planet embedded in a PPD with a given physical properties would impose on the gas (e.g. Fung et al. 2014; Duffell 2015; Kanagawa et al. 2015, 2016). The associated analytical criteria approximate these simulations and link planet masses to gap depth and width. Following
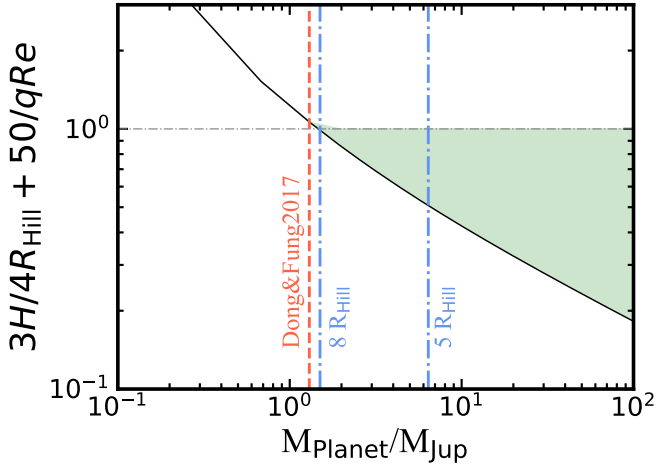
Fig. 5. Crida et al. (2006) criterion of Eq. (2) applied to the gap-opening planet mass in the PPD around HD 97048. The green-shaded area shows the masses at which a planet would carve a deep gap in the gas at the observed location of 127 au (Ginski et al. 2016), assuming a disk viscosity parameter of $\alpha = 10^{-3}$. The vertical blue dash-dotted lines correspond to a planet creating a depleted region of width $5\,R_{\rm Hill}$ and $8\,R_{\rm Hill}$, following Eq. (1). The red dashed line indicates the estimated perturber mass by Dong & Fung (2017b), using a detailed hydrodynamical + radiative transfer simulation of the gap morphological parameters.

Dong & Fung (2017b), the gap depth in gas is given by

$$\frac{\Sigma_0(r_{\rm min,\Sigma})}{\Sigma(r_{\rm min,\Sigma})} = 0.043\, q^2 \left(\frac{H}{r}\right)^{-5} \alpha^{-1} + 1 \tag{3}$$

and the normalised and dynamical gap width is found to scale only with the local disk aspect ratio as

$$\frac{r_{\rm in,\Sigma} - r_{\rm out,\Sigma}}{r_{\rm min,\Sigma}} = 5.8\, \frac{H}{r}, \tag{4}$$

where q, α, and H/r are the mass ratio between the companion and the host star, the accretion disk viscosity parameter (Shakura & Sunyaev 1973), and the disk aspect ratio, respectively. The locations ($r_{\rm in,\Sigma}$ and $r_{\rm out,\Sigma}$) are the edges of the gap, defined as the positions where the surface density reaches the mean of the minimum $\Sigma(r_{\rm min,\Sigma})$ and undepleted $\Sigma_0(r_{\rm min,\Sigma})$ surface density. These morphological parameters also need to be connected to the observed parameters in scattered-light images. 2D and 3D hydrodynamical simulations coupled to radiative transfer calculations show that this translation depends mostly on the inclination of the disk and the angular resolution and sensitivity of the observations (Szulágyi et al. 2018). Using this formulation, Dong & Fung (2017b) obtained a value for the mass of the perturber of $1.3\,M_{\rm Jup}$ for $\alpha = 10^{-3}$ and $H/r = 0.056$ (see Fig. 5). This is in agreement with the derivation using Crida's criterion, although it does not always have to be the case, as Eqs. (3) and (4) are accommodated to each specific gap morphology, unlike Eq. (2). When comparing the two criteria at the depth assumed by Crida, this latter prescription tends to derive a higher planet mass (see e.g. Fig. 12 in Bergez-Casalou et al. 2020).

We finally apply the gap-opening Hill radius criterion of Eq. (1) to this gap. A scaling factor of $k = 8$ is necessary to simulate the mass derived by Dong & Fung (2017b). We find that for LkCa 15, the ~90 au gap in TW Hya and HD 169142, we are also able to approximate the simulations of Dong & Fung (2017b) with $k \sim 8$–10. However, a $k > 10$ scaling is necessary to account for their derived masses in the ~78 au gap around RX

J1615.3-3255 and the ~22 au gap in TW Hya, which is related to the individual gap morphology that the Hill radius approximation does not account for. To give an insight into the uncertainties involved when applying this basic Hill radius approximation, variations in the k factor from 8 to 12 can be translated to a perturber's mass estimate between ~1.5 to $0.5\,M_{\rm Jup}$ for the gap we are considering in HD 97048. Likewise, another source of uncertainty is the viscosity α assumed by the models; Dong & Fung (2017a) find that the mass of the perturber changes by a factor of 10 between the two extreme values they considered, from $\alpha = 10^{-4}$ to $\alpha = 10^{-2}$.

Here, we take from the literature the location of all the gaps between rings and within cavities found in the SPHERE scattered-light images of our PPD sample, and assume that one planet at that location opens a gap that scales with $k = 8$. This also includes PDS 70, for which we ignore the two giant planets detected in its cavity for the rest of the analysis in order to be used as a point of reference and comparison with other systems. An individual brief discussion of each system and its substructures is provided in Appendix A, together with a very simple representation of their scattered-light appearance and the locations at which we locate the perturbers (Fig. A.1). If the gap minimum location is not explicitly calculated in the literature, we place the putative planet in the centre between a pair of rings. When the region between the star and the inner ring is depleted down to the coronagraphic IWA in the μm-sized dust, we treat it as a cavity. In these cases we locate the planet at one-half the distance between the star and the rim, which does not necessarily need to be the case in a real scenario. We also treat the outer rings of PDS 70 and LkCa 15 as cavities, although non-resolved inner disk signals in the small dust are detected close to the mask. With this prescription we seek to account for a global estimate of planet masses in real observations of gaps that are not fully depleted.

Figure 6 shows the planet masses derived through the Hill radius approximation with $k = 8$. The perturbers are located at the gap minimum within the cavities and between rings of the PPDs in our sample. When derivations from simulations exist in the literature, we adopt those. They are marked with an asterisk in the figure. We also include the latest simulated planet masses and locations that explain the spirals seen in HD 36112 (Baruteau et al. 2019) and HD 135344B (Dong & Fung 2017a). In this section, we do not consider three systems, CQ Tau, HD 100546, and HD 139614, because they have complicated structures with no clear gaps, or because no simulated planets creating the spirals exist. From the figure, two different populations of perturbers seem to arise: more massive 3–10 $M_{\rm Jup}$ objects that create big cavities, and a more sparse population of planets creating gaps within rings in the ~0.01–1 $M_{\rm Jup}$ regime. The latter are all massive enough to potentially create detectable gaps in PPDs (e.g. Bitsch et al. 2018). We note that these derived perturbers are objects that could migrate and evolve (e.g. Lodato et al. 2019), and so the mass–position diagram of Fig. 6 is not directly comparable to the population observed by the indirect methods. In Fig. 7 these masses are compared to the derived 5σ mass detection limits at the proposed location of the perturber, computed for the different starting luminosities after deprojecting the 2D mass sensitivity maps.

These two figures suggest the following: (1) our sensitivities do not reach masses for planets creating the gaps in the disk population with rings; (2) planet masses needed to create the observed cavities are in general larger than those in the gaps between rings, unless the assumption that only one planet induces the cavity is incorrect; (3) if hot-start models are a good
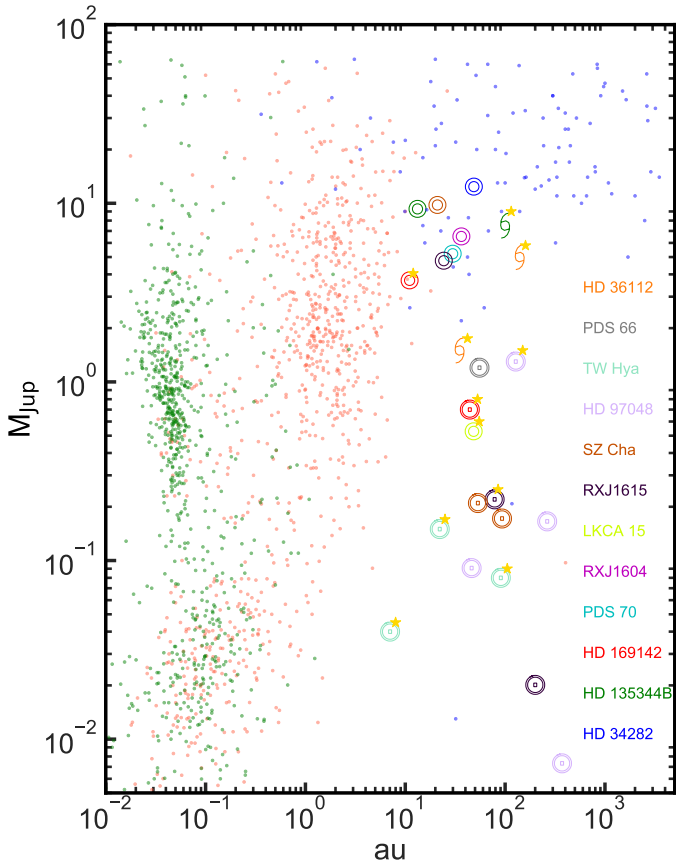
Fig. 6. Underlying population of potential perturbers derived from PPD substructures in the SPHERE scattered-light images. For planets in the gaps between rings (circles with inner dots) and planets in cavities (circles), these values are estimated using a proportionality factor of $8\,R_{Hill}$ to account for the mass that would create the observed width in the scattered-light gap (Eq. (1)). When the gap morphology in scattered light was taken into account, planet masses are taken from detailed simulations in the literature for $\alpha = 10^{-3}$, and are marked with an asterisk. Simulated planets creating spiral features are also included as spiral symbols (see references in the Appendix A and see also Fig. A.1). The distributions of confirmed planets in the exoplanets.eu catalogue are shown as small dots: green (radial velocity discoveries), orange (transits), and blue (imaging).

Fig. 7. Population of perturbers from Fig. 6 compared to our derived 5σ deprojected mass sensitivities at their location, which is shown on the right side of the figure. SPHERE/IRDIS with AMES-DUSTY, BEX-HOT, and BEX-WARM initial starts are shown as red, orange, and blue bars, respectively. The dashed lines correspond to SPHERE/IFS-ASDI contrasts and AMES-DUSTY post-formation luminosity.

representation of the initial planet luminosities, we could be close to a detection in several systems, omitting the extinction due to the potential surrounding circumplanetary and circumstellar material. To date, two giant planets in PDS 70 are the only bona fide detections, which might imply the presence of currently undetected lower-mass companions in these systems, or that other physical mechanisms may be responsible for the formation of the cavity, such as dead-zones, MHD winds, instabilities, or grain growth at snow lines (Flock et al. 2015; Pinilla et al. 2016; Takahashi & Inutsuka 2016; Cieza et al. 2016); and (4) planet masses creating gaps within scattered-light rings are consistent with the population of undetected companions that is emerging from the high-resolution ALMA data (see Fig. 21 in Zhang et al. 2018).

Figure 8 shows a histogram version of the results in Fig. 7. We can see that there are eight cases (i.e. the first bin) where these putative planets with the hottest starts could be detectable: six in cavities (HD 34282, Sz Cha, HD 135344B, RX J1604, PDS 70 and RX J1615) and two creating spiral patterns (HD 135344B and HD 36112). Additionally, three perturbers might be close to

a detection (defined here as less than half an order of magnitude away in mass, forming the second bin) in the cavity of HD 169142 and the gaps between rings in HD 97048 and PDS 66. Table 4 shows these most promising systems where perturbers can be found based on this analysis. For the perturbers in cavities very close to the coronagraphic mask, spatial resolution and projection effects can also affect the detection. Overall, these results suggest that planets may not be the only way of creating substructures, given the current number of detections, unless cold initial conditions represent a better description of their luminosity, which is unlikely according to Marleau et al. (2019b).

4.2. Gap opening mass from scattered light-millimetre continuum comparison

In this section, we derive planet masses for the systems in which resolved rings and/or cavities exist both in SPHERE scattered light and in ALMA millimetre continuum observations (see

Table 4. Perturbers close to detection based on the mass estimates of Sect. 4.1.

ID	Gap	Location (au)	Planet mass ($M_{\rm Jup}$)	AMES-DUSTY ($M_{\rm Jup}$)	BEX-HOT ($M_{\rm Jup}$)
HD 34282	In-cavity	44	11.7	10.0	11.8
SZ Cha	In-cavity	19	9.3	4.1	6.2
HD 135344B	In-cavity	12	8.8	5.8	7.0
HD 135344B	Spiral	100	5–10	3.8	4.9
RX J1604	In-cavity	33	6.2	5.1	6.4
HD 36112	Spiral	140	5.0	4.6	5.8
PDS 70	In-cavity	27	4.9	4.1	5.3
RX J1615	In-cavity	22	4.5	2.5	4.3
HD 169142	In-cavity	10	3.5	8.1	9.5
HD 97048	In-rings	127	1.3	3.9	5.5
PDS 66	In-rings	55	1.2	2.5	3.5

Notes. Perturbers that, according to the estimations of Fig. 7, are the most promising to be found. PDS 70 treated as planet-less here. Planet masses in gaps and creating the spiral patterns are taken as described in Fig. 6. The columns AMES-DUSTY and BEX-HOT are our derived SPHERE detection limits (best of ANDROMEDA/IRDIS and ASDI/IFS) using the AMES-DUSTY and BEX-HOT models (see Sect. 3). References for the locations of the perturbers can be found in Appendix A. See also Fig. A.1 for a sketch of these morphologies.
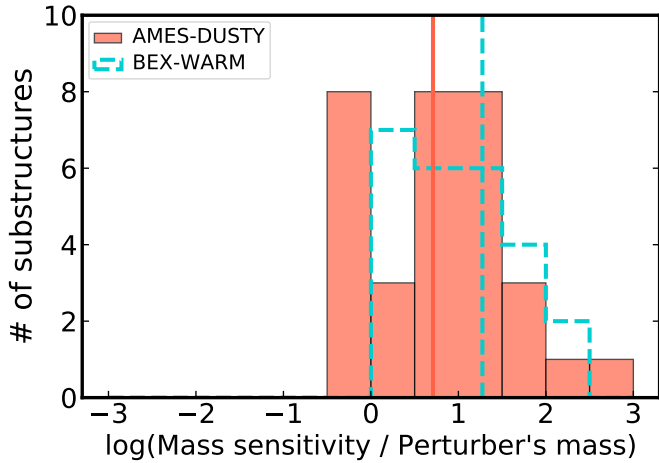
Fig. 8. Histogram of the difference between estimated planet masses that create substructures in our PPD sample and the derived contrast mass limits at their location. The vertical lines show the median value for each mass–luminosity relationship. Units are in orders of magnitude in mass.

Table 5). SPHERE PDI observations trace the small dust coupled to the gas in a PPD, while ALMA data probe mm-sized dust grains settled in the disk midplane. For this reason, the pressure bump created by the presence of a planetary-mass companion can leave its imprint in the different appearance of the disk at different wavelengths. In general, large grains will accumulate more effectively at the peak of the gas pressure, as no drag force exists in the pressure bump, making the gas rotate near or exactly at Keplerian velocity, while μm-sized dust is well-coupled to the gas and moves along with it. This effect creates a spatial difference in the cavity sizes observed in the millimetre continuum with ALMA and in polarised scattered light, which is dependent on the planet mass and disk location.

de Juan Ovelar et al. (2013) simulated the radial distribution of the dust due to the presence of 1, 9, and 15 $M_{\rm Jup}$ giant planets located at 20, 40 and 60 au around a solar-mass star, after 3 Myr of evolution and α viscosity of 10^{-3}. We use their functional form of the ratio in the cavity size seen in μm- and mm-sized dust for

a given planet mass

$$f(M_{\rm p}) = c \left(\frac{M_{\rm p}}{M_{\rm Jup}} \right)^{\Gamma}, \tag{5}$$

where $f(M_{\rm p})$ is defined as the ratio of the location of the scattered-light inner edge of the cavity seen with SPHERE/ZIMPOL to the peak in 850 μm flux with ALMA, $c \sim 0.85$, and $\Gamma \sim [-0.22, -0.18, -0.16]$ respectively for planet orbital radii $R_{\rm p} = [20, 40, 60]$.

The location of the scattered-light inner edge is usually not provided from the observations. Following Villenave et al. (2019), we derive for each gap a minimum planet mass ($M_{\rm p}$ (min)), assuming that the scattered-light edge is at the one-half distance between the peak of the disk in PDI and the gap minimum, and a maximum planet mass ($M_{\rm p}$ (max)), taking the scattered-light edge as the position of the peak in PDI. We use as $R_{\rm p}$ the location of the gap in scattered light. In the cases where $f(M_{\rm p})$ is close to 1, the predicted mass is below 1 $M_{\rm Jup}$. This regime is outside the range of the simulations, and observational uncertainties in the derivation of the peak locations would be of critical importance. We thus limit ourselves to the 1–15 $M_{\rm Jup}$ mass range, and treat these values as the upper and lower thresholds of the resulting planet masses outside these limits. We also extrapolate the value of Γ to the location of the gaps in our sample, assuming that it behaves linearly at distances >60 au within the 1–15 $M_{\rm Jup}$ mass range.

From this approximation, we see in Fig. 9 that perturbers within large cavities are close to detection under AMES-DUSTY conditions (RX J1604, PDS 70 and HD 135344B). Again, planets in the gaps between a pair of rings such as HD 97048 and HD 169142 seem to be at least about half an order of magnitude lower in mass than currently detectable. The derived masses for these systems are also in good agreement with those derived in the previous section from Hill radii or estimated from simulations that relate the mass to the morphological features of the gaps (see Tables 4 and 5). In Fig. 10, we show this difference for those substructures carved by 1–15 $M_{\rm Jup}$ planets. For most of these perturbers, the mass derived using the ALMA observations is typically within a factor of ∼0.4 and 1.5 of that obtained via the Hill radius criterion. We do not show here the potential planet creating the gap at ∼45 au around HD 97048, as only an

Table 5. Perturber masses creating SPHERE/PDI-ALMA substructures.

Host ID	Min PDI (au)	Peak PDI (au)	Peak (mm) (au)	M_p (min) (M_{Jup})	M_p (max) (M_{Jup})	AMES-DUSTY (M_{Jup})	BEX-HOT (M_{Jup})
HD 135344B	12	24	51	12.5	>15	5.8	7.0
RX J1604	33	66	90	2.2	9.5	5.1	6.4
PDS 70	27	54	75	2.1	8.5	4.1	5.3
HD 34282	44	89	138	4.8	>15	10.0	11.8
HD 169142	10	20	25	1.2	4.1	8.1	9.5
LKCA 15	43	59	66	<1	1.6	9.7	12.3
HD 97048	127	188	189	<1	1.2	3.9	5.5
HD 169142	44	63	64	<1	1.1	3.4	4.1
HD 97048	45	54	55	<1	<1	5.6	7.5

Notes. Minimum and maximum mass of the perturbers, M_p (min) and M_p (max), respectively, calculated using Eq. (5). The derived detection limits at the perturber's location using AMES-DUSTY and BEX-HOT tracks (best of ANDROMEDA/IRDIS and ASDI/IFS) are shown in the last two columns. References for the location of the substructures can be found in Appendix A.
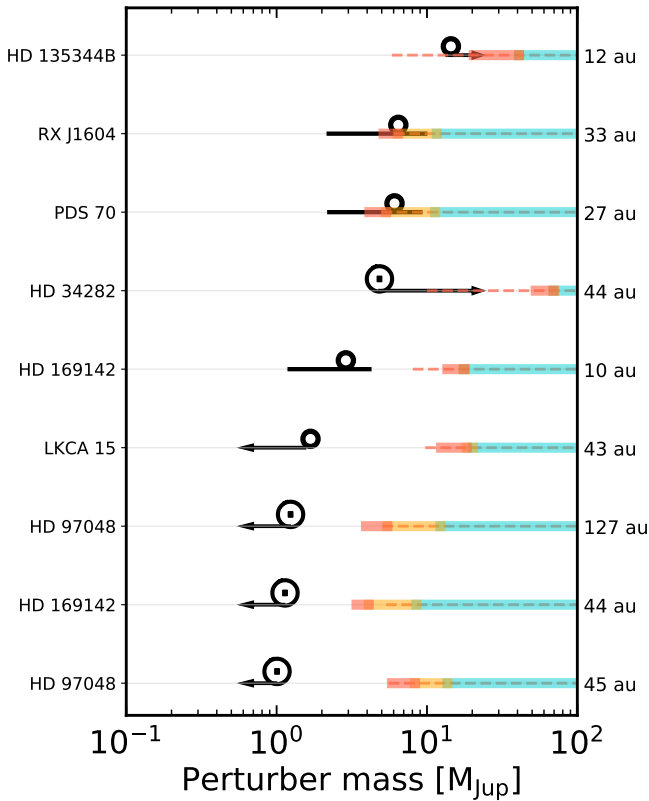
Fig. 9. Predicted masses from the de Juan Ovelar et al. (2013) prescription (black) using SPHERE scattered-light images and ALMA millimetre peak emission. Arrows are used when the estimated mass limit is either lower than $1\,M_{Jup}$ or higher than $15\,M_{Jup}$ (i.e. outside the regime of Eq. (5)). ANDROMEDA/IRDIS detection limits with AMES-DUSTY, BEX-HOT, and BEX-WARM initial starts are shown as red, orange, and blue bars, respectively. The dashed lines correspond to ASDI/IFS AMES-DUSTY detection limits.

Fig. 10. Difference in the estimated mass of the perturbers of Fig. 6 (M_{GM}), calculated using the gap morphological features observed only in scattered light, and those calculated via de Juan Ovelar et al. (2013), which compares the cavity sizes in scattered light and the millimetre continuum ($M_{Ovelar+2013}$). The only assumed uncertainties are those linked to the location of the scattered-light inner edge of Eq. (5).

upper limit can be constrained with Eq. (2), but both approaches yield a planet mass well below $1\,M_{Jup}$.

5. Discussion

5.1. Why is the current detection rate so low?

These homogeneously derived detection limits in mass have clear implications on the detectability of potential companions

in very young PPDs. If planets creating substructures in PPDs have a very hot start, our results suggest that the majority of them are probably less massive than $\sim 4\,M_{Jup}$ (see Fig. 2). However, the mass detection limits are affected by a factor of ~ 3 if planets were formed via cold core-accretion models, which is a consequence of the very young age of our sample. If we compare our sensitivities to the SPHERE/SHINE survey (see Fig. B.1 in Vigan et al. 2021), we see that their limits are moved towards higher masses, as SHINE is comprised mostly of stars of age $\sim 50\,$Myr that are members of nearby young moving groups (Desidera et al. 2021). Moreover, the luminosities at the beginning of formation have less impact on their final results

because the hot and cold populations tend to converge to almost identical luminosities at ages >50 Myr (Baraffe et al. 2003; Marley et al. 2007; Spiegel & Burrows 2012; Mordasini et al. 2017; Linder et al. 2019), contrary to our results for <10 Myr targets.

The detection limits derived in this work are in line with the non-detection of sub-Jupiter-mass planets in gaps within rings, but our derivation of planet masses in cavities seem to suggest the presence of ∼5 $M_{\rm Jup}$ companions, which would be close to a detection in several systems. Even so, only two bona fide giant protoplanets have been imaged, both of them in the cavity of PDS 70 (Mesa et al. 2019), although some other candidates have been proposed in HD 100546 (Brittain et al. 2014; Quanz et al. 2015), LkCa 15 (Sallum et al. 2015) and HD 169142 (Gratton et al. 2019), but remain uncertain (e.g. Rameau et al. 2017; Currie et al. 2019).

An explanation for the low detection rate of giant planets in PPDs could be that the perturber masses are overestimated. The problem of estimating masses from the observed morphologies in the dust is still complex; current analytical equations describing the gap can only be used after making several assumptions, such as the disk temperature, viscosity, gas accretion effects, and dust evolution or migration. Simulations of planet–disk interactions also need to account for more complex and realistic thermodynamics that account for the cooling efficiency of the disk, which would impact the morphology and the number of gaps that a planet can produce (e.g. Szulágyi 2017; Miranda & Rafikov 2020). Including more physics in the theoretical simulations in fact suggests that the derived masses by locally isothermal relations might be underestimated. Under the isothermal assumption, for a given planet mass the gap is wider than in the case where the disk does not cool rapidly. This implies that the derived masses by current isothermal relations might be underestimating the real mass of the perturbers, as even small planets could open up wide gaps. The same conclusion is found if gas accretion is taken into account (Bergez-Casalou et al. 2020).

If the planet is not on a circular or coplanar orbit, the dynamical mass estimates (see Eqs. (3) and (4)) would also be modified; for example, a planet on an eccentric orbit may open a wider but shallower gap (Muley et al. 2019). This assumption on the planet orbit is mostly justified on the basis of parameter restriction on the theoretical simulations, and it is not clear how this could affect a large sample. For instance, PDS 70b is found to be on an eccentric orbit of $e \sim 0.17$ (Wang et al. 2021), and the presence of misaligned inner disks, such the one around J1604 in this sample, might point to the presence of a companion in a highly inclined orbit (Mayama et al. 2012; Pinilla et al. 2018).

Nevertheless, our masses derived via gap morphology and those calculated with ALMA data seem to agree, and are probably representative of the order of magnitude of the perturber mass. For the special case of PDS 70, which we treated as a planet-less PPD, the derived mass of a single perturber carving its cavity at 27 au has a mass of 4.9 $M_{\rm Jup}$ using the Hill radii prescription, or between 2.1–8.5 $M_{\rm Jup}$ following Eq. (5). This is comparable to the mass of PDS 70b or c (both of ∼5 $M_{\rm Jup}$) at 23 and 30 au, respectively (Mesa et al. 2019). If accretion luminosity is taken into account as a contributor to the observed luminosity, the mass of PDS 70b decreases to about 1 $M_{\rm Jup}$ (Stolker et al. 2020). Assuming that PDS 70c follows a similar pattern, the combined mass of the two planets is in the range 2–3 $M_{\rm Jup}$. This may indeed be affecting the current number of detections in cavities; as claimed by Dodson-Robinson & Salyk (2011), several undetected lower-mass planets of mass ≥1 $M_{\rm Jup}$ might be creating the large holes in optically thin transition disks, and

not a single very massive companion. Assuming the presence of more than one perturber inside a cavity would greatly affect the mass estimates of Eq. (1), which leads to the assumption that Rim systems have more massive planets than Ring systems, with the only exception of LkCa 15. There is not yet enough information in scattered light to derive the mass of multiplanet systems in cavities from their observed morphology, but simulated scattered-light images of cavities opened by multiple Jovian planets seem to resemble the observations (see Figs. 5 and 7 in Dong et al. 2015).

Another possibility is that some (or most) of these planets reradiate the energy influx generated during the gas accretion shock, and consequently are better described by cold starts, which is not theoretically supported (Szulágyi & Mordasini 2017; Marleau et al. 2019b). In this scenario, in direct imaging surveys we would have detected only those born with high entropies, but the bulk of the planets that create substructures, which would be formed by a cold process, remain undetected after the PPD phase (Vigan et al. 2021). However, planets of <10 Myr may still be actively accreting the material that resides within the gap, inside the circumplanetary disk from which the planet feeds. In the case of a cold formation pathway, the resulting accretion luminosity radiated away by these planets would be easily detectable, and could be even brighter than the planet irradiation itself, especially at near-IR wavelengths (Zhu 2015; Szulágyi et al. 2019; Sanchis et al. 2020). Brittain et al. (2020) circumvent this apparent inconsistency by proposing episodical accretion of circumplanetary disks, in which accretion outbursts where planets could be detected only occur during 2% of the runaway accretion phase.

Nonetheless, the number of systems with resolved depleted cavities or spiral patterns in scattered light which also have high-contrast total intensity observations is still low, as shown in this work. Detection probabilities are also hampered by projection effects in PPDs that are not seen face-on, especially at close semi-major axes (see the detection probability maps in Appendix C), and the emission of disk residuals in the ADI data, which are sometimes difficult to distinguish from real companions (Sissa et al. 2018; Gratton et al. 2019). Further observations of young cavity-hosting disks in both polarised and ADI modes would help constrain all these different scenarios, and to understand whether other theoretical interpretations not related to the presence of perturbers might be necessary to explain the various morphologies, such as effective dust growth at snowlines (Pinilla et al. 2017), variations in the ionisation level of the gas (Flock et al. 2015), or photoevaporation winds (Owen et al. 2012).

5.2. Extinction effects

Throughout this study we have assumed that the observed emission of these young planets will not be affected by the presence of disk material along the line of sight. However, all forming planets have to be surrounded by circumplanetary material regardless of their mass, since they still accrete. As long as they do it, there has to be material around to accrete from, which means that planetary atmospheres can well be extincted, shifting the emission to longer wavelengths. If an extended cloud of material around the planet exists, observations might not even be detecting the planet itself, but the reprocessed emission of the dust (e.g. Szulágyi et al. 2019; Stolker et al. 2020). As seen for PDS 70b, even with 1–5 μm photometry and spectroscopy, the protoplanet nature of these objects makes it difficult to disentangle the intrinsic planet emission from that of the circumplanetary environment, and whether the dust reddening the spectrum is

located in the planet's atmosphere, in the circumplanetary envelope or in the circumstellar disk (Müller et al. 2018; Haffert et al. 2019; Mesa et al. 2019; Christiaens et al. 2019; Stolker et al. 2020; Wang et al. 2020).

If the bulk of the perturbers creating the scattered-light gaps between rings have masses that are a fraction of that of Jupiter, as the results suggest, they might not open deep enough gaps to clear all the disk material, and the extinction could indeed completely impede their detection in the near-infrared. According to 3D high-resolution hydrodynamical simulations of disk–planet interaction by Sanchis et al. (2020), their emission (intrinsic and accretion shock luminosity) can be highly attenuated by the surrounding dust (about ~13 mag in H band and ~4 in L at locations of ~100 au for a 1 M_{Jup} companion), depending on disk aspect ratio, surface densities, viscosities, dust processing, and planet formation parameters. However, when the undepleted disk surface density is low, even low-mass objects seem to suffer little extinction at any distance in the PPD. For instance, in PDS 70 the infrared extinction has an incidence in H band only for planets <2 M_{Jup} at distances of <40 au, and due to the very low surface density of the PPD around CQ Tau (Ubeira Gabellini et al. 2019) extinction is only somewhat relevant for 1 Jupiter-mass planets within 20 au, with an L-band extinction of 0.3 mag (Sanchis et al. 2020). For the three potential sub-Jupiter planets carving the gaps in TW Hya, van Boekel et al. (2017) estimated an extinction in H band of about 2 magnitudes during the late detached phase, and for the same system Sanchis et al. (2020) increased the mass upper limits obtained by Ruane et al. (2017) only from 1 to 2 M_{Jup}, when extinction is taken into account. Maire et al. (2017) also found that the detection mass limits beyond the spirals in HD 135344B might be underestimated by not more than 2 M_{Jup}. These results suggest that, depending on the individual system, the derived mass sensitivities to low-mass perturbers depleting the µm-sized dust may be too optimistic, with a critical effect in dense PPDs, and a low or moderate influence in PPDs with a lower surface density.

Perturbers with masses higher than 4 M_{Jup} will not suffer substantially from extinction in any band or distance, according to Sanchis et al. (2020), even for very dense disks, because the material is cleared within the gap. However, those simulations do not count with a well-resolved planet vicinity, which means that the density of material is lower than it would be with a fully resolved CPD (see Szulágyi et al. 2019). In addition, they assume a face-on configuration of the disk, whereas the circumstellar disk could distort the vision of the planet for inclined systems (e.g. Szulágyi & Garufi 2021). For these reasons, these values can be better considered as lower limits for extinction.

In summary, we expect that the emission originating in the potential >4 M_{Jup} planets carving the cavities will not be heavily obscured, as is the case for PDS 70b (Mesa et al. 2019). Hence, in the majority of situations perturbers susceptible of being substantially extinced (>2 mag) in the H and K bands are in any case too low mass ($\leq$2 M_{Jup}) to be detected by the SPHERE detection limits, while more massive planets that are within SPHERE's reach would probably suffer less obscuration. A more detailed luminosity estimate of the forming planets would consist in coupling evolutionary models of 'naked' planets (as in Fig. 7) with individual high-resolution hydrodynamical simulations of the disk.

5.3. Potential for future detection

Based on the results of the two previous sections, giant planets in cavities seem to be within the reach of current high-contrast
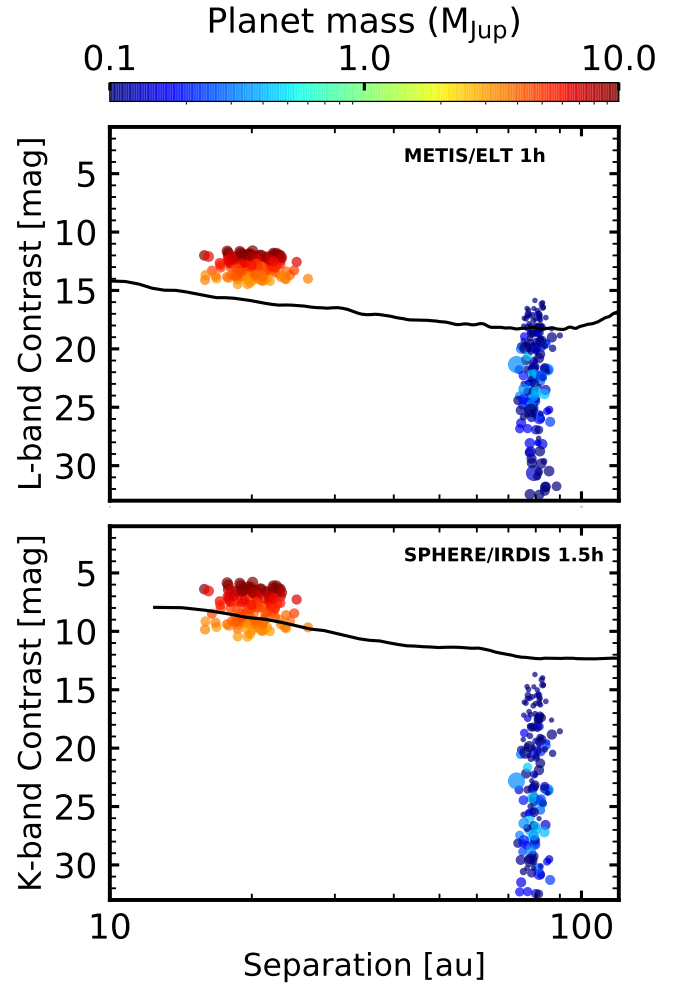

Fig. 11. Contrast magnitudes for 8 Myr planets in the NG76 population synthesis model (Emsenhuber et al. 2020, 2021). Two populations of 0.05–0.5 M_{Jup} and 3–10 M_{Jup} planets are artificially located at 80 and 20 au, respectively. Estimated extinction coefficients are from Sanchis et al. (2020) (see text). The METIS contrast curve is from Carlomagno et al. (2020), and the SPHERE limits correspond to the derived contrast in this work for RX J1604, which we adopt as a representative host star. Small random shifts in separation are applied for a better visibility of the populations, and dot sizes are connected to planet radius.

imagers such as SPHERE, and constitute the most promising places for imaging a giant planet. Planets carving the gaps between rings, however, have masses of about ~0.1 M_{Jup}, similar to those of the undetected planetary-mass companions responsible for the gaps in mm-sized dust seen in high-resolution ALMA observations in the DSHARP survey (Zhang et al. 2018) and in the Taurus star-forming region (Long et al. 2018). Even without considering the presence of extinction, this level of contrast is unattainable for current instruments (see Figs. 7 and 8).

If the surface density depletions are indeed caused by the presence of embedded sub-Jupiter-mass companions, their detection might be more favourable at longer wavelengths. A future instrument that would enable their detection is the Mid-Infrared E-ELT Imager and Spectrograph (METIS; Brandl et al. 2014). The top panel of Fig. 11 shows the detection limit in L band of METIS after 1 h of integration, compared to two different populations of synthetic planets; 0.05–0.5 M_{Jup} companions that might potentially be creating gaps in the outer disks, which we locate at 80 au, and more massive 3–10 M_{Jup} objects opening up cavities at 20 au. Planet parameters have been obtained

from the synthetic population model NG76[2] (Emsenhuber et al. 2020, 2021) for a median age of our sample of 8 Myr. We considered objects with an atmosphere and in the detached evolutionary phase or later, and calculated their approximate brightnesses in L band assuming that the planets radiate as black bodies, following van Boekel et al. (2017). The simulated contrast curve was taken from Carlomagno et al. (2020), and uses a ring-apodised vortex coronagraph (RAVC). To calculate the contrast between the host star and the synthetic population, we assume a host star like RX J1604, an early K dwarf located at the median distance of our sample. We also include the extinction coefficients derived by Sanchis et al. (2020) for an unperturbed surface density of $\Sigma = 127\,\mathrm{g\,cm^{-2}}$, consistent with the densest disks in star forming regions; we take their values for a $5\,M_{\mathrm{Jup}}$ planet at 20 au (see their Table A.2) and for a $1\,M_{\mathrm{Jup}}$ planet at 100 au (see their Table A.4), and apply them to the in-cavity and in-ring planets, respectively. The sizes of the dots are correlated with the planet radius.

We see that METIS will be able to detect giant planets forming the resolved cavities in scattered light with masses $>3\,M_{\mathrm{Jup}}$, and possibly also a small fraction of those in the gaps between rings in the systems where extinction is low. In the lower panel of Fig. 11 the same calculations are made for SPHERE/IRDIS in the K band. As expected, it shows that the current instrumentation is within the limit of providing giant planet images within cavities, but the bulk of the sub-Jupiter-mass planets are out of reach.

This implies that the use of complementary pipelines and the weather conditions during the observations may now have a critical effect in detecting giant planets for which instruments such as SPHERE are close to the detection limits (see e.g. Fig. A.1 in Keppler et al. 2018). Obtaining the best possible observing conditions for the most promising systems in Table 4, together with detailed and varied reduction schemes, could be the most favourable case for a new protoplanet detection in a PPD in the near future.

Direct coronagraphic imaging at long wavelengths ($>3\,\mu\mathrm{m}$) with the *James Webb* Telescope (JWST) will also be useful for detecting and characterising young Saturn-like planets at projected distances $>1''$ (e.g. Beichman et al. 2010). For nearby and large PPDs, JWST may be able to provide the most constringent mass limits of planets creating substructures at hundreds of au, down to $\sim0.2\,M_{\mathrm{Jup}}$ around dwarf K and M host stars (Carter et al. 2021), and also to characterise their atmospheric compositions and planet parameters, which would in turn shed light on the formation pathways (Linder et al. 2019).

Finally, another way to look for these perturbers is to detect hydrogen emission lines, such as Hα, originating in the shock-heated gas during the accretion of disk material (Aoyama & Ikoma 2019). If detected, this emission constitutes the main observational signature of the ongoing formation of a substellar object (Eriksson et al. 2020). Observations of PPDs with SPHERE/ZIMPOL and MUSE have so far been unable to detect planetary-mass companions around PPD hosts other than the pair around PDS 70, despite reaching potential sensitivities down to $1\,M_{\mathrm{Jup}}$ (Haffert et al. 2019; Zurlo et al. 2020).

6. Conclusions

In this work, we have presented a homogeneous ADI data reduction of 15 PPDs observed with SPHERE which are characterised by rings, cavities, or spirals in scattered light. We provided detection limits to low-mass companions creating these substructures, and studied the difference between the current SPHERE mass limits and the estimated sensitivity that would be needed to achieve a detection in these systems. The main results of this paper can be summarised as follows:

1. We find that the detection limits in our PPD sample (K and earlier-type host stars of $\lesssim10$ Myr) are greatly affected by the assumed initial luminosity of the perturber, with median sensitivities that vary for the hottest AMES-DUSTY starts from ~9 to $4\,M_{\mathrm{Jup}}$, respectively for perturbers in close (~10 au) and wide (~100s of au) orbits. If a cold start based on core accretion formation is considered, these detection limits are deteriorated by a factor of ~3, and sensitivities to perturbers barely reach the planetary-mass regime. An assessment of the detection limits in mass for each individual system can be found in Appendix B;

2. We performed an estimation of the mass of the currently undetected perturbers via three approaches: (1) literature simulations based on the scattered-light morphology of the disk; (2) gap width in scattered light proportional to the Hill radius of the planet; and 3) location of the scattered-light cavity compared to its radius in ALMA millimetre continuum observations. Assuming that one perturber is responsible for creating one substructure, the underlying population of planets is located between ~10–400 au and within a mass range of 0.01–$1\,M_{\mathrm{Jup}}$ for gaps between rings, and more massive companions of up to ~3–$10\,M_{\mathrm{Jup}}$ in cavities and spirals. They represent the potential objects that would be needed to create the current substructures seen in young disks, which have so far no direct correspondence to any detected population of exoplanets;

3. We compared the estimated masses to the obtained detection limits at the perturbers' positions. We find that SPHERE is about one order of magnitude away in mass from detecting the majority of planets creating the gaps between scattered-light rings. If the presence of material attenuating the planet emission is important, this difference could be more pronounced. Perturbers creating cavities tend to be more massive, and current SPHERE detection limits seem to be good enough for potential detections, consistent with the discovery of two giant planets in PDS 70;

4. In addition to PDS 70, we find that the cavities in RX J1604, RXJ1615, Sz Cha, HD 135344B and HD 34282 are the most promising systems for a future direct detection of giant planets. Perturbers of the order of a Jupiter mass might also be found in between the rings of PDS 66 and HD 97048;

5. Future imaging instruments such as ELT/METIS and the JWST may be able to explore the hottest population of planets depleting the μm-sized dust between rings. These surveys will help to constrain the initial luminosities of the perturbers and link planet masses to gap morphologies;

6. Current dynamical mass constraints assume the presence of a single planet on a coplanar and circular orbit in an isothermal disk. This premise might not be universally realistic, which could lead to overestimated mass derivations. Further work in this area exploring a larger parameter space in the properties of planets would help reduce these uncertainties on the planet masses creating substructures in the scattered light.

---

[2] `https://dace.unige.ch/populationAnalysis/?populationId=ng76`

References

Allard, F., Hauschildt, P. H., Alexander, D. R., Tamanai, A., & Schweitzer, A. 2001, ApJ, 556, 357

Andrews, S. M., Huang, J., Pérez, L. M., et al. 2018, ApJ, 869, L41

Aoyama, Y., & Ikoma, M. 2019, ApJ, 885, L29

Aoyama, Y., Ikoma, M., & Tanigawa, T. 2018, ApJ, 866, 84

Aoyama, Y., Marleau, G.-D., Mordasini, C., & Ikoma, M. 2021, Spectral appearance of the planetary-surface accretion shock: Global spectra and hydrogen-line profiles and fluxes

Asensio-Torres, R., Currie, T., Janson, M., et al. 2019, A&A, 622, A42

Astropy Collaboration (Robitaille, T. P., et al.) 2013, A&A, 558, A33

Astropy Collaboration (Price-Whelan, A. M., et al.) 2018, AJ, 156, 123

Avenhaus, H., Quanz, S. P., Garufi, A., et al. 2018, ApJ, 863, 44

Bae, J., Pinilla, P., & Birnstiel, T. 2018, ApJ, 864, L26

Baraffe, I., Chabrier, G., Barman, T. S., Allard, F., & Hauschildt, P. H. 2003, A&A, 402, 701

Baraffe, I., Homeier, D., Allard, F., & Chabrier, G. 2015, A&A, 577, A42

Baruteau, C., Barraza, M., Pérez, S., et al. 2019, MNRAS, 486, 304

Beichman, C. A., Krist, J., Trauger, J. T., et al. 2010, PASP, 122, 162

Benisty, M., Juhasz, A., Boccaletti, A., et al. 2015, A&A, 578, A6

Bergez-Casalou, C., Bitsch, B., Pierens, A., Crida, A., & Raymond, S. N. 2020, A&A, 643, A133

Beuzit, J. L., Vigan, A., Mouillet, D., et al. 2019, A&A, 631, A155

Bitsch, B., Morbidelli, A., Johansen, A., et al. 2018, A&A, 612, A30

Bonavita, M., Chauvin, G., Desidera, S., et al. 2012, A&A, 537, A67

Bonnefoy, M., Marleau, G. D., Galicher, R., et al. 2014, A&A, 567, A9

Brandl, B. R., Feldt, M., Glasse, A., et al. 2014, in Society of Photo-Optical Instrumentation Engineers (SPIE) Conference Series, 9147, Ground-based and Airborne Instrumentation for Astronomy V, eds. S. K. Ramsay, I. S. McLean, & H. Takami, 914721

Brandt, G. M., Brandt, T. D., Dupuy, T. J., Li, Y., & Michalik, D. 2021, AJ, 161, 179

Bressan, A., Marigo, P., Girardi, L., et al. 2012, MNRAS, 427, 127

Brittain, S. D., Carr, J. S., Najita, J. R., Quanz, S. P., & Meyer, M. R. 2014, ApJ, 791, 136

Brittain, S. D., Najita, J. R., Dong, R., & Zhu, Z. 2020, ApJ, 895, 48

Cantalloube, F., Mouillet, D., Mugnier, L. M., et al. 2015, A&A, 582, A89

Carlomagno, B., Delacroix, C., Absil, O., et al. 2020, J. Astron. Telescopes Instrum. Syst., 6, 035005

Carter, A. L., Hinkley, S., Bonavita, M., et al. 2021, MNRAS, 501, 1999

Cazzoletti, P., van Dishoeck, E. F., Pinilla, P., et al. 2018, A&A, 619, A161

Chabrier, G., Baraffe, I., Allard, F., & Hauschildt, P. 2000, ApJ, 542, 464

Chauvin, G., Desidera, S., Lagrange, A. M., et al. 2017, A&A, 605, L9

Choi, J., Dotter, A., Conroy, C., et al. 2016, ApJ, 823, 102

Christiaens, V., Casassus, S., Absil, O., et al. 2019, MNRAS, 486, 5819

Cieza, L. A., Casassus, S., Tobin, J., et al. 2016, Nature, 535, 258

Claudi, R. U., Turatto, M., Gratton, R. G., et al. 2008, in Society of Photo-Optical Instrumentation Engineers (SPIE) Conference Series, 7014, Ground-based and Airborne Instrumentation for Astronomy II, eds. I. S. McLean & M. M. Casali, 70143E

Crida, A., Morbidelli, A., & Masset, F. 2006, Icarus, 181, 587

Currie, T., Marois, C., Cieza, L., et al. 2019, ApJ, 877, A3

de Boer, J., Salter, G., Benisty, M., et al. 2016, A&A, 595, A114

de Boer, J., Langlois, M., van Holstein, R. G., et al. 2020, A&A, 633, A63

de Boer, J., Ginski, C., Chauvin, G., et al. 2021, A&A 649, A25

de Juan Ovelar, M., Min, M., Dominik, C., et al. 2013, A&A, 560, A111

Delorme, P., Meunier, N., Albert, D., et al. 2017, in SF2A-2017: Proceedings of the Annual Meeting of the French Society of Astronomy and Astrophysics,

eds. C. Reylé, P. Di Matteo, F. Herpin, E. Lagadec, A. Lançon, Z. Meliani, & F. Royer, Di

Desidera, S., Chauvin, G., Bonavita, M., et al. 2021, A&A, 651, A70

Dodson-Robinson, S. E., & Salyk, C. 2011, ApJ, 738, 131

Dohlen, K., Langlois, M., Saisse, M., et al. 2008, in Society of Photo-Optical Instrumentation Engineers (SPIE) Conference Series, 7014, Ground-based and Airborne Instrumentation for Astronomy II, eds. I. S. McLean & M. M. Casali, 70143L

Dong, R., & Fung, J. 2017a, ApJ, 835, 38

Dong, R., & Fung, J. 2017b, ApJ, 835, 146

Dong, R., Zhu, Z., & Whitney, B. 2015, ApJ, 809, 93

Dong, R., Liu, S.-y., Eisner, J., et al. 2018, ApJ, 860, 124

Dotter, A., Chaboyer, B., Jevremović, D., et al. 2008, ApJS, 178, 89

Drążkowska, J., Alibert, Y., & Moore, B. 2016, A&A, 594, A105

Duffell, P. C. 2015, ApJ, 807, L11

Dullemond, C. P., & Penzlin, A. B. T. 2018, A&A, 609, A50

Durisen, R. H., Boss, A. P., Mayer, L., et al. 2007, in Protostars and Planets V, eds. B. Reipurth, D. Jewitt, & K. Keil, 607

Emsenhuber, A., Mordasini, C., Burn, R., et al. 2020, A&A, submitted [arXiv:2007.05562]

Emsenhuber, A., Mordasini, C., Burn, R., et al. 2021, A&A, in press, https://doi.org/10.1051/0004-6361/202038553

Eriksson, S. C., Asensio Torres, R., Janson, M., et al. 2020, A&A, 638, A6

Fedele, D., van den Ancker, M. E., Henning, T., Jayawardhana, R., & Oliveira, J. M. 2010, A&A, 510, A72

Flock, M., Ruge, J. P., Dzyurkevich, N., et al. 2015, A&A, 574, A68

Fortney, J. J., Marley, M. S., Hubickyj, O., Bodenheimer, P., & Lissauer, J. J. 2005, Astron. Nachr., 326, 925

Francis, L., & van der Marel, N. 2020, ApJ, 892, 111

Fung, J., & Dong, R. 2015, ApJ, 815, L21

Fung, J., Shi, J.-M., & Chiang, E. 2014, ApJ, 782, 88

Gaia Collaboration (Prusti, T., et al.) 2016, A&A, 595, A1

Gaia Collaboration (Brown, A. G. A., et al.) 2021, A&A 649, A1

Galicher, R., Boccaletti, A., Mesa, D., et al. 2018, A&A, 615, A92

Garufi, A., Quanz, S. P., Schmid, H. M., et al. 2016, A&A, 588, A8

Garufi, A., Benisty, M., Pinilla, P., et al. 2018, A&A, 620, A94

Garufi, A., Avenhaus, H., Pérez, S., et al. 2020, A&A, 633, A82

Ginski, C., Stolker, T., Pinilla, P., et al. 2016, A&A, 595, A112

Gonzalez, J. F., Laibe, G., & Maddison, S. T. 2017, MNRAS, 467, 1984

Grady, C. A., Schneider, G., Hamaguchi, K., et al. 2007, ApJ, 665, 1391

Gratton, R., Ligi, R., Sissa, E., et al. 2019, A&A, 623, A140

Haffert, S. Y., Bohn, A. J., de Boer, J., et al. 2019, Nat. Astron., 3, 749

Hashimoto, J., Dong, R., Kudo, T., et al. 2012, ApJ, 758, A19

Hauschildt, P. H., Allard, F., & Baron, E. 1999, ApJ, 512, 377

Hendler, N. P., Pinilla, P., Pascucci, I., et al. 2018, MNRAS, 475, L62

Huang, J., Andrews, S. M., Cleeves, L. I., et al. 2018, ApJ, 852, 122

Isella, A., Natta, A., Wilner, D., Carpenter, J. M., & Testi, L. 2010, ApJ, 725, 1735

Jin, S., Isella, A., Huang, P., et al. 2019, ApJ, 881, 108

Kanagawa, K. D., Muto, T., Tanaka, H., et al. 2015, ApJ, 806, L15

Kanagawa, K. D., Muto, T., Tanaka, H., et al. 2016, PASJ, 68, 43

Keppler, M., Benisty, M., Müller, A., et al. 2018, A&A, 617, A44

Keppler, M., Teague, R., Bae, J., et al. 2019, A&A, 625, A118

Langlois, M., Gratton, R., Lagrange, A. M., et al. 2021, A&A 651, A71

Ligi, R., Vigan, A., Gratton, R., et al. 2018, MNRAS, 473, 1774

Linder, E. F., Mordasini, C., Mollière, P., et al. 2019, A&A, 623, A85

Lodato, G., Dipierro, G., Ragusa, E., et al. 2019, MNRAS, 486, 453

Long, F., Pinilla, P., Herczeg, G. J., et al. 2018, ApJ, 869, 17

Long, F., Herczeg, G. J., Harsono, D., et al. 2019, ApJ, 882, 49

Maire, A. L., Stolker, T., Messina, S., et al. 2017, A&A, 601, A134

Marleau, G.-D., Coleman, G. A. L., Leleu, A., & Mordasini, C. 2019a, A&A, 624, A20

Marleau, G.-D., Mordasini, C., & Kuiper, R. 2019b, ApJ, 881, 144

Marley, M. S., Fortney, J. J., Hubickyj, O., Bodenheimer, P., & Lissauer, J. J. 2007, ApJ, 655, 541

Marois, C., Lafrenière, D., Doyon, R., Macintosh, B., & Nadeau, D. 2006, ApJ, 641, 556

Mayama, S., Hashimoto, J., Muto, T., et al. 2012, ApJ, 760, L26

Mayama, S., Akiyama, E., Panić, O., et al. 2018, ApJ, 868, L3

Mesa, D., Gratton, R., Zurlo, A., et al. 2015, A&A, 576, A121

Mesa, D., Keppler, M., Cantalloube, F., et al. 2019, A&A, 632, A25

Miranda, R., & Rafikov, R. R. 2020, ApJ, 904, 121

Mordasini, C., Marleau, G. D., & Mollière, P. 2017, A&A, 608, A72

Muley, D., Fung, J., & van der Marel, N. 2019, ApJ, 879, L2

Müller, A., Keppler, M., Henning, T., et al. 2018, A&A, 617, L2

Muro-Arena, G. A., Benisty, M., Ginski, C., et al. 2020, A&A, 635, A121

Murphy, S. J., Joyce, M., Bedding, T. R., White, T. R., & Kama, M. 2021, MNRAS, 502, 1633

Nowak, M., Lacour, S., Lagrange, A. M., et al. 2020, A&A, 642, L2
Okuzumi, S., Momose, M., Sirono, S.-i., Kobayashi, H., & Tanaka, H. 2016, ApJ, 821, 82
Owen, J. E., Clarke, C. J., & Ercolano, B. 2012, MNRAS, 422, 1880
Pérez, S., Casassus, S., Baruteau, C., et al. 2019, AJ, 158, 15
Pineda, J. E., Szulágyi, J., Quanz, S. P., et al. 2019, ApJ, 871, 48
Pinilla, P., Benisty, M., & Birnstiel, T. 2012, A&A, 545, A81
Pinilla, P., de Juan Ovelar, M., Ataiee, S., et al. 2015, A&A, 573, A9
Pinilla, P., Flock, M., Ovelar, M. d. J., & Birnstiel, T. 2016, A&A, 596, A81
Pinilla, P., Pohl, A., Stammler, S. M., & Birnstiel, T. 2017, ApJ, 845, 68
Pinilla, P., Benisty, M., de Boer, J., et al. 2018, ApJ, 868, 85
Pinte, C., Price, D. J., Ménard, F., et al. 2018, ApJ, 860, L13
Pinte, C., van der Plas, G., Ménard, F., et al. 2019, Nat. Astron., 3, 1109
Pohl, A., Benisty, M., Pinilla, P., et al. 2017, ApJ, 850, 52
Qi, C., Ho, P. T. P., Wilner, D. J., et al. 2004, ApJ, 616, L11
Quanz, S. P., Amara, A., Meyer, M. R., et al. 2015, ApJ, 807, 64
Rameau, J., Follette, K. B., Pueyo, L., et al. 2017, AJ, 153, 244
Reggiani, M., Christiaens, V., Absil, O., et al. 2018, A&A, 611, A74
Ribas, Á., Bouy, H., & Merín, B. 2015, A&A, 576, A52
Rice, W. K. M., Armitage, P. J., Wood, K., & Lodato, G. 2006, MNRAS, 373, 1619
Riols, A., Lesur, G., & Menard, F. 2020, A&A, 639, A95
Ruane, G., Mawet, D., Kastner, J., et al. 2017, AJ, 154, 73
Sallum, S., Follette, K. B., Eisner, J. A., et al. 2015, Nature, 527, 342
Sanchis, E., Picogna, G., Ercolano, B., Testi, L., & Rosotti, G. 2020, MNRAS, 492, 3440
Shakura, N. I., & Sunyaev, R. A. 1973, A&A, 500, 33
Sissa, E., Gratton, R., Garufi, A., et al. 2018, A&A, 619, A160
Sokal, K. R., Deen, C. P., Mace, G. N., et al. 2018, ApJ, 853, 120
Spiegel, D. S., & Burrows, A. 2012, ApJ, 745, 174
Stolker, T., Dominik, C., Avenhaus, H., et al. 2016, A&A, 595, A113
Stolker, T., Marleau, G. D., Cugno, G., et al. 2020, A&A, 644, A13
Szulágyi, J. 2017, ApJ, 842, 103

Szulágyi, J., & Garufi, A. 2021, MNRAS 506, 73
Szulágyi, J., & Ercolano, B. 2020, ApJ, 902, 126
Szulágyi, J., & Mordasini, C. 2017, MNRAS, 465, L64
Szulágyi, J., Morbidelli, A., Crida, A., & Masset, F. 2014, ApJ, 782, 65
Szulágyi, J., Plas, G. v. d., Meyer, M. R., et al. 2018, MNRAS, 473, 3573
Szulágyi, J., Dullemond, C. P., Pohl, A., & Quanz, S. P. 2019, MNRAS, 487, 1248
Takahashi, S. Z., & Inutsuka, S.-i. 2016, AJ, 152, 184
Taki, T., Fujimoto, M., & Ida, S. 2016, A&A, 591, A86
Teague, R., Bae, J., Bergin, E. A., Birnstiel, T., & Foreman-Mackey, D. 2018, ApJ, 860, L12
Teague, R., Bae, J., Huang, J., & Bergin, E. A. 2019, ApJ, 884, L56
Thalmann, C., Janson, M., Garufi, A., et al. 2016, ApJ, 828, L17
Ubeira Gabellini, M. G., Miotello, A., Facchini, S., et al. 2019, MNRAS, 486, 4638
Uyama, T., Muto, T., Mawet, D., et al. 2020, AJ, 159, 118
van Boekel, R., Henning, T., Menu, J., et al. 2017, ApJ, 837, 132
van der Marel, N., Cazzoletti, P., Pinilla, P., & Garufi, A. 2016, ApJ, 832, 178
van der Plas, G., Ménard, F., Canovas, H., et al. 2017a, A&A, 607, A55
van der Plas, G., Wright, C. M., Ménard, F., et al. 2017b, A&A, 597, A32
van Holstein, R. G., Girard, J. H., de Boer, J., et al. 2020, A&A, 633, A64
Vigan, A. 2020, vlt-sphere: Automatic VLT/SPHERE data reduction and analysis
Vigan, A., Fontanive, C., Meyer, M., et al. 2021, A&A 651, A72
Villenave, M., Benisty, M., Dent, W. R. F., et al. 2019, A&A, 624, A7
Wang, J. J., Graham, J. R., Dawson, R., et al. 2018, AJ, 156, 192
Wang, J. J., Ginzburg, S., Ren, B., et al. 2020, AJ, 159, 263
Wang, J. J., Vigan, A., Lacour, S., et al. 2021, AJ, 161, 148
Whipple, F. L. 1972, in From Plasma to Planet, ed. A. Elvius, 211
Williams, J. P., & Cieza, L. A. 2011, ARA&A, 49, 67
Zhang, S., Zhu, Z., Huang, J., et al. 2018, ApJ, 869, L47
Zhu, Z. 2015, ApJ, 799, 16
Zurlo, A., Cugno, G., Montesinos, M., et al. 2020, A&A, 633, A119

Appendix A: Notes on individual targets

HD 135344B. Disk with spiral and inner cavity. PDI resolved in Stolker et al. (2016), showing an inner cavity at ~24 au and a clear spiral pattern, from which we take the inclination and PA. To explain the spiral arms, many different predictions exist involving the presence of a massive companion. For instance, Dong & Fung (2017a) suggest a giant ~5–10 $M_{\rm Jup}$ planet on a wide orbit ~100 AU to explain the arm contrast in scattered light, which is in agreement with the results of the symmetry-based method by Fung & Dong (2015). van der Marel et al. (2016) proposes another possibility with a planet located inside the inner gap at 30 au that produces a vortex farther out, which gives rise to the spiral pattern. Here, we simply consider the outer massive planet from Dong & Fung (2017a) (calculated with a distance to the target of 140 au, instead of our updated 135 au value from GAIA-EDR3). We also consider a planet located in the middle of the 24 au cavity using the Hill radius approach. Although very close to the coronagraphic mask, this distance corresponds to roughly 0.1″, at which position we obtain the sensitivity limit. ALMA observations from Cazzoletti et al. (2018) show a mm-dust cavity at 50 au and a crescent peaking at ~80 au.

HD 139614. This is a complicated system in scattered light, with shadows and a system of misaligned inner rings that are probably due to the presence of a misaligned companion. A bright ring is seen down to ~16 au or 0.12″ (Muro-Arena et al. 2020), together with three arcs at larger separations that might be caused by variations in the scale height profile. No clear gaps in the scattered light are detected, and for this reason no perturber is derived for this system. Mass detection limits can be found in Appendix B. We adopt the inclination and position angle of the outer disk. ALMA data are not available yet.

HD 97048. Four gaps and rings are seen in scattered light by Ginski et al. (2016), whose values we adopt after GAIA-EDR3 distance correction. For gap 2 we assume the derivation from Dong & Fung (2017b) of 1.3 $M_{\rm Jup}$ for $\alpha = 10^{-3}$ (although we note that they used a distance to the system of 158 pc), which is in line with the kinematic detection of a 2–3$M_{\rm Jup}$ planet candidate in that same gap at ~130 au (Pinte et al. 2019). The inclination and position angle are from the same study. Rings 1 and 2 have direct correspondence in the millimetre at 55 au (peak at 0.3″, van der Plas et al. 2017b) and 189 au (Francis & van der Marel 2020).

PDS 66. This scattered-light disk is part of the DARTSS-S survey (Avenhaus et al. 2018). A clear ring-like structure can be seen at a best-fit value of 85 au. There is no significant deficiency in polarised signal close to the coronagraph; a bright compact region out to 25 au is detected, which rules out the presence of a highly depleted inner cavity of μm-sized grains. We thus classify this object as Ring and put the putative planet in the faint region between the compact inner structure and the ring (i.e. at 55 au), which in turn corresponds to an apparent discontinuity seen in the data. The inclination and position angle are from this work. To our knowledge there is no high-resolution ALMA data for this system yet.

LkCa 15. This is a transitional disk resolved by SPHERE in Thalmann et al. (2016), with the outer disk located at ~58 au and a gap minimum at 43 au, where we locate the planet. Inclination and position angle from this work. A perturber of mass 0.5 $M_{\rm Jup}$ for $\alpha = 10^{-3}$ seems necessary to carve the cavity in μm-sized

dust (Dong & Fung 2017b). ALMA observations show a dust cavity of 66 au (Jin et al. 2019).

RX J1615.3-3255. This is a transitional disk showing three different rings in PDI at 44, 166, and 232 au (de Boer et al. 2016; Avenhaus et al. 2018). Ellipses are fit to these three substructures, providing locations and geometry. We classify this disk as Ring, but treat the inner rim as a cavity in terms of planet-carving structure in Hill radii. The gap at ~78 au (labelled 'G' in de Boer et al. 2016) can be created by a planet of mass 0.2 $M_{\rm Jup}$ for $\alpha = 10^{-3}$, according to Dong & Fung (2017b). The third planet is put in the middle of the location between the two outer rings. There is also an additional ring-like structure between the two inner rings seen by Avenhaus et al. (2018), only seen on the north-eastern side, which we do not consider here. ALMA observations also show three rings at closer separations than seen in the small dust (Benisty, M. priv. comm), so we do not use their position to derive planet masses.

HD 169142. The *J*-band PDI data by Pohl et al. (2017) reveal a nearly face-on disk with a double-ring structure with a central cavity of ~20 au. The two rings are fitted with an ellipse, whose parameters we adopt here. Using dust evolution models, they found that two giant planets of 3.5 and 0.7 $M_{\rm Jup}$ can reproduce the disk structure in SPHERE/PDI and the location and width of the gap, which we adopt. A dedicated SPHERE ADI study of Gratton et al. (2019) finds a potential accreting planet candidate between the two rings at 38 au, detected in reflected polarised light and with a mass of ~2 $M_{\rm Jup}$ for an age of 5 Myr. A point-like structure is also at ~10 au by Ligi et al. (2018). This disk is classified as Ring, even though we treat the inner ring as a cavity. The system has been observed by ALMA at high resolution, showing the inner cavity and the ring at 25 au, and the outer ring composed of three narrow components. In this comparison between scattered-light and millimetre emission, we link the outer ring in scattered light to the central narrow ring component resolved by ALMA and peaking at 64 au (Pérez et al. 2019).

HD 100546. This PPD presents a complex structure of rings, arms and spirals. It was first imaged in polarimetric scattered light with the ZIMPOL instrument of SPHERE in the optical by Garufi et al. (2016), and later with IRDIS in the near-infrared by Sissa et al. (2018). A ~13 au (0.12″) cavity close to the coronagraphic mask is detected, together with a complex structure of wrapped arms beyond 1″ that may form a spiral, and three additional small arm-like structures closer in. The presence of two planetary-mass companions has also been suggested (e.g. Brittain et al. 2014; Quanz et al. 2015), but their nature is still debated (Rameau et al. 2017). We derive no perturber masses for this system given its intricate morphology in scattered light, but present detection limits in Appendix B. High-resolution ALMA observations by Pineda et al. (2019) detect a ring-like structure between 20–40 au, which can be reproduced with a vortex and two rings peaking at 21 and 30 au. An unresolved, central compact emission is also detected. We take the inclination and position angle from that study.

PDS 70. This transitional disk hosts two giant planets carving a wide gap of 54 au (Keppler et al. 2018; Müller et al. 2018; Haffert et al. 2019). For our calculations, in order to provide a comparison, we do not consider that this system hosts the planets at those positions. An inner bright structure below 17 au is observed, but not resolved. We thus put our potential planet in the centre of the outer ring at 27 au. Inclination and PA are taken

from Hashimoto et al. (2012). Follow-up high-resolution observations with ALMA emission found the outer cavity peaking at 75 au in the dust continuum, and an inner ring at 10 au (Keppler et al. 2019; Francis & van der Marel 2020).

Sz Cha. This disk has been observed in IRDIS *H*-band DPI mode. It is characterised by three different rings with semi-major axes between 0.2″ and 0.6″. We adopt here the ellipse fitting parameters derived by Hagelberg et al. (priv. comm.), and classify the disk as Ring, treating the inner one as a cavity. We are not aware of current observations of this object in the millimetre emission with enough resolution to observe substructures.

HD 34282. Scattered-light image from de Boer et al. (2021). Two rings seem to be well-fitted, the inner one (rim R2) at a semi-major axis of ∼89 au. The second one after scale height deprojection seems to be more coincident with a single-armed spiral. There seem to be no simulations of planets causing the spiral in scattered light yet. The inclination and PA are from this paper. The ALMA data from van der Plas et al. (2017a) show a ring in the continuum extending from 75 au to 359 au, but peaking at the deprojected radius of 138 au. According to their work, a 50 $M_{\rm Jup}$ object at 0.1″ (∼30 au) could explain the ALMA ring. We thus classify this object as Spiral, and use the inner rim to derive a planetary mass inside the scattered-light cavity via Hill radius, which will be similar to the ALMA planet candidate.

RX_J1604.3-2130A. This transition disk shows variable dips and a ring peaking at 66 au in scattered light (Pinilla et al. 2018). The dips might be caused by the presence of an inner misaligned ring. The cavity is wider in the ALMA observations, which reveal an elliptical fit to the outer disk peaking at 90 au in the dust continuum (Mayama et al. 2018).

HD 36112. This transitional disk with an inner eccentric cavity is resolved in the millimetre wavelengths out to ∼50 au in deprojected distance (Dong et al. 2018), but not in PDI with SPHERE down to ∼15 au (Benisty et al. 2015). Scattered-light observations, however, show a pair of spirals with a large opening angle from ∼0.25–0.45″. The object is thus classified as Spiral, and the inclination and position angle are taken from Isella et al. (2010). Baruteau et al. (2019) have simulated planet masses and locations that create these substructures. They take into account previous upper limits on planet sensitivities (e.g. Reggiani et al. 2018), and reproduce the spirals in scattered light and the submillimetre crescent substructure with two planets of mass 1.5 $M_{\rm Jup}$ and 5 $M_{\rm Jup}$ located at 35 au and 140 au (for a distance of 160 pc), inside and outside the spirals, respectively. We assume these simulated planets as the ones creating the substructures and compare them to our sensitivities. As no resolved inner cavity is seen with SPHERE, we do not use this object for the ALMA-scattered light comparison.

TW Hya. SPHERE shows a face-on disk with three wide but shallow gaps in the μm-sized dust at approximately 7, 22, and 90 au (van Boekel et al. 2017). This work derives the planet masses carving these non fully depleted gaps from their depths following Duffell (2015). We scale these values for $\alpha = 10^{-3}$ and obtain 0.04 $M_{\rm Jup}$ for the innermost gap. We rely on Dong & Fung (2017b) for the masses of the perturbers causing the two outer gaps, 0.15 and 0.08 $M_{\rm Jup}$. We treat the three gaps as rings, as ALMA observations in the submillimetre show a ring at ∼2 au. The ∼22 au depression is also observed by ALMA in the surface brightness of the continuum (e.g. Huang et al. 2018), but no clear correspondence with brightness peaks can be done between the millimetre and scattered light. Even though van Boekel et al. (2017) assumed a face-on disk, here we take the inclination and position angle derived by Qi et al. (2004) from CO imaging of the outer disk.

CQ Tau. SPHERE PDI data shows a spiral pattern extending up to ∼0.4″, but a cavity is not resolved outside the coronagraphic mask (Benisty et al., in prep.). NIRC2 observations in *L* band have excluded the presence of giant planetary-mass companions down to 5 $M_{\rm Jup}$ outside the spiral region (Uyama et al. 2020). Ubeira Gabellini et al. (2019) report ALMA data showing a depleted cavity with a rim at ∼57 au. The inclination and position angle are taken from this work.
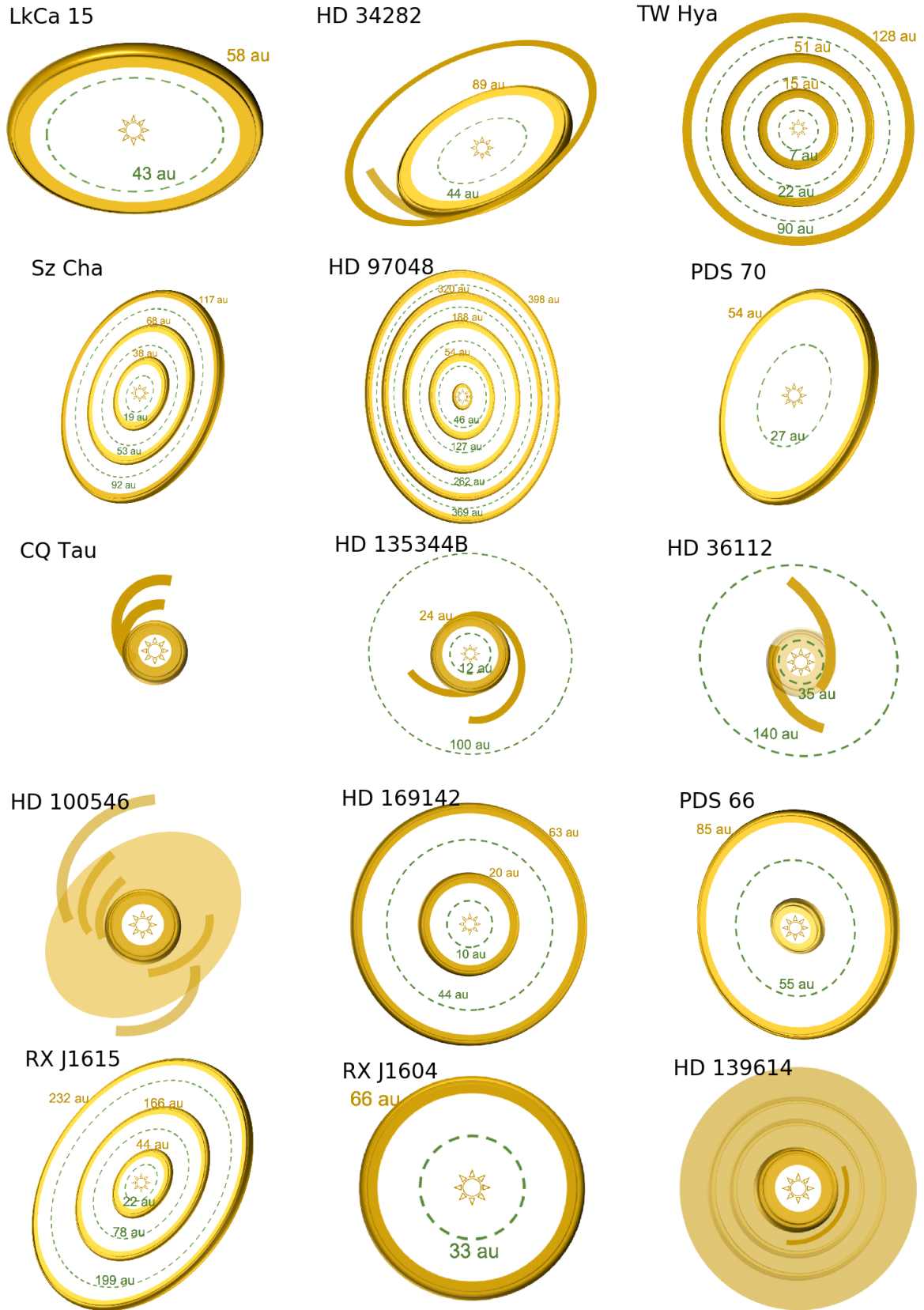
Fig. A.1. Sketch representation of the scattered light appearance of the PPD sample. Included are only the gaps and substructures considered to have been created by perturbers in Sect. 4. The adopted locations of these perturbers are shown as green dashed curves. Scattered-light rings are shown as thick rings, while arms and spiral patterns are shown as flat curled curves. The disks are projected according to their inclination and position angle values listed in Table 2. Also included are HD 100546, HD 139614 and CQ Tau for completeness, although no clear gaps or simulated planets creating the spiral pattern exist.

Appendix B: Deprojected mass sensitivity curves

Here, we show the detection limits in mass for all the targets analysed in this work, with three different initial luminosity conditions. Deprojected separations were obtained as explained in Sect. 2. The location of the various substructures observed in both scattered light and millimetre continuum (see Appendix A) are also overplotted.
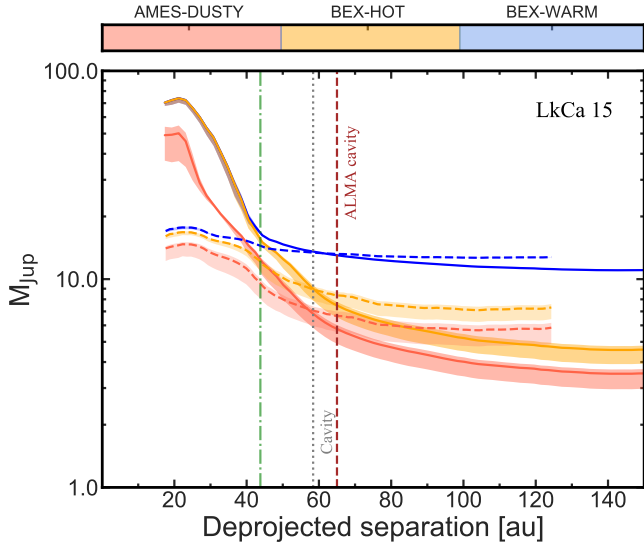
Fig. B.1. 5σ sensitivity to planet masses in LkCa 15. The different initial luminosities for the derived age in Table 1 are shown as red, orange, and blue curves respectively for the AMES-DUSTY, BEX-HOT, and BEX-WARM models. Thick curves correspond to the ANDROMEDA IRDIS limits, and dashed curves show the IFS-ASDI performance using the SPHERE mode in Table 2. The shaded regions encompass the upper and lower limits of the age uncertainty. SPHERE PDI substructures are shown in grey as vertical dotted lines, and the observed peaks in ALMA dust continuum are shown as brown dashed lines. Only ALMA rings with correspondence to scattered-light substructures are shown. The green dash-dotted vertical lines indicate reported gap locations in PDI.
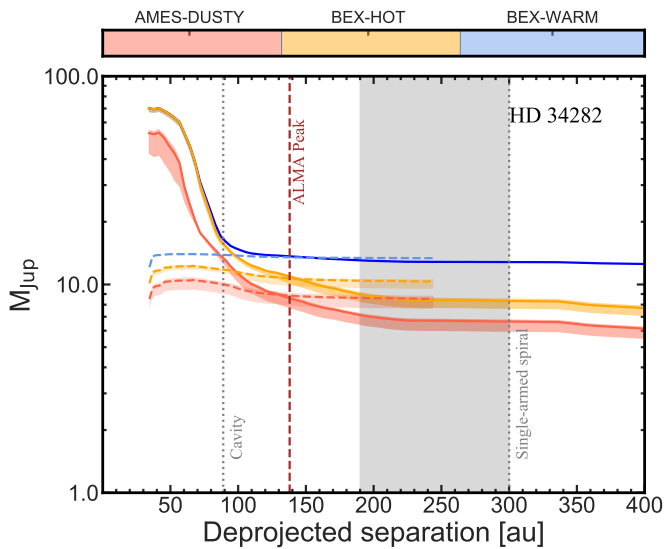
Fig. B.2. 5σ sensitivity to planet masses in HD 34282 (see Fig. B.1). The vertical grey shaded region corresponds to the spatial extension of the spiral feature.
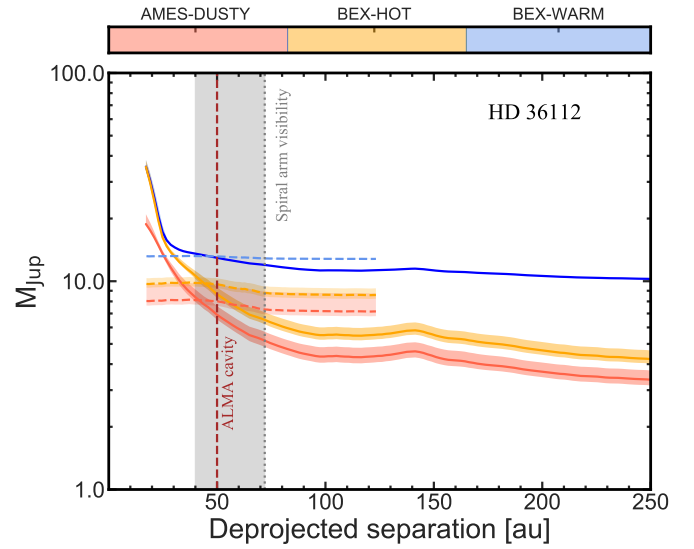
Fig. B.3. 5σ sensitivity to planet masses in HD 36112 (see Fig. B.2).
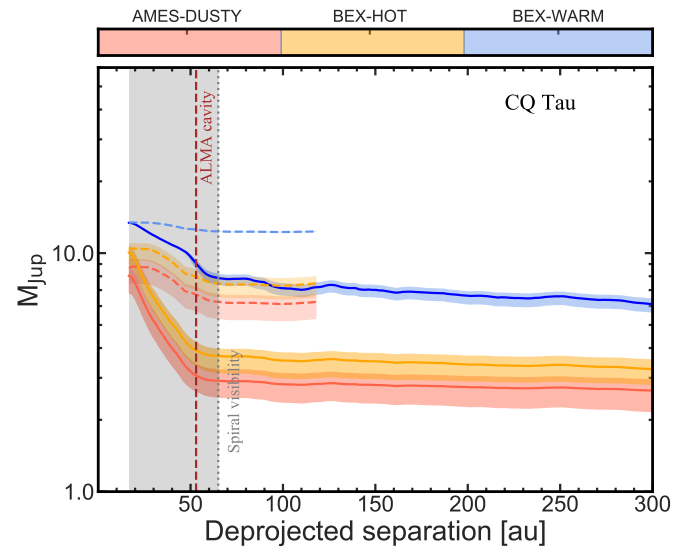
Fig. B.4. 5σ sensitivity to planet masses in CQ Tau (see Fig. B.2).
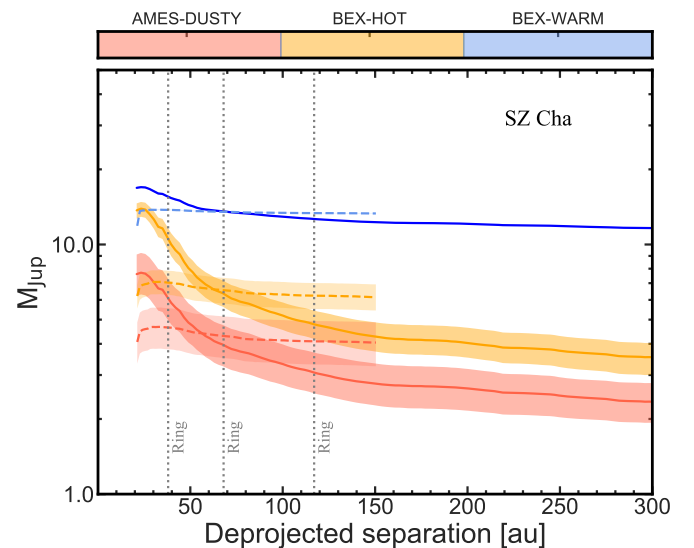
Fig. B.5. 5σ sensitivity to planet masses in Sz Cha (see Fig. B.1).
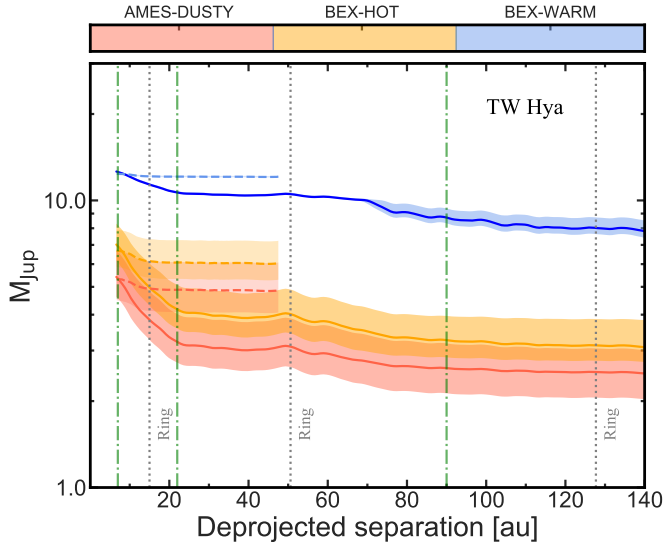
Fig. B.6. 5σ sensitivity to planet masses in TW Hya (see Fig. B.1).
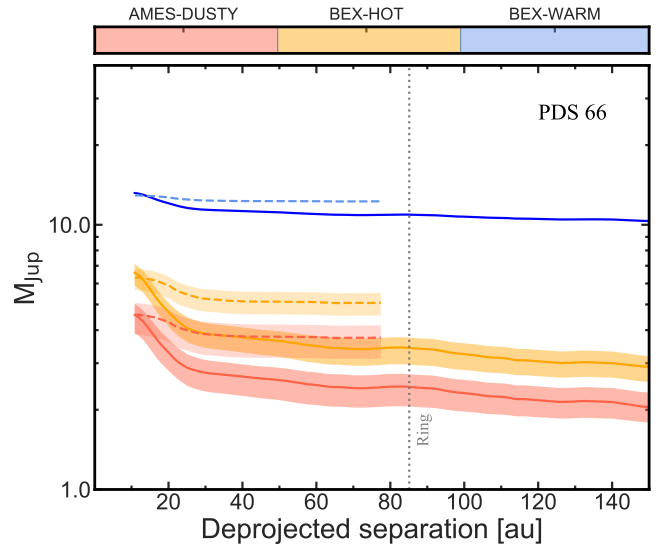
Fig. B.9. 5σ sensitivity to planet masses in PDS 66 (see Fig. B.1).
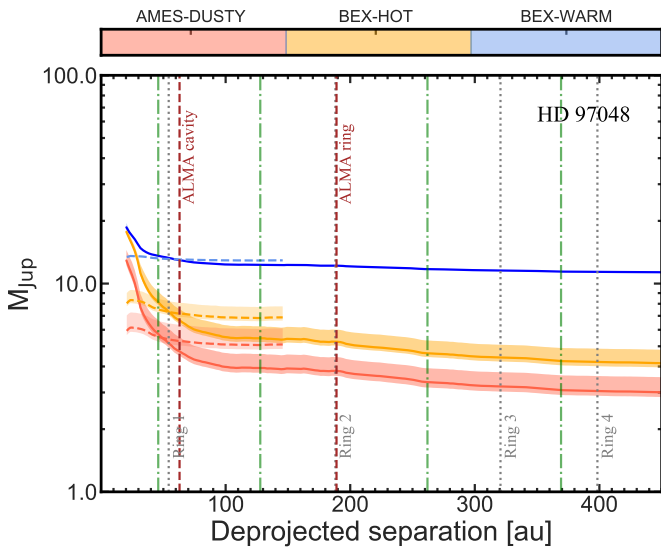
Fig. B.7. 5σ sensitivity to planet masses in HD 97048 (see Fig. B.1).
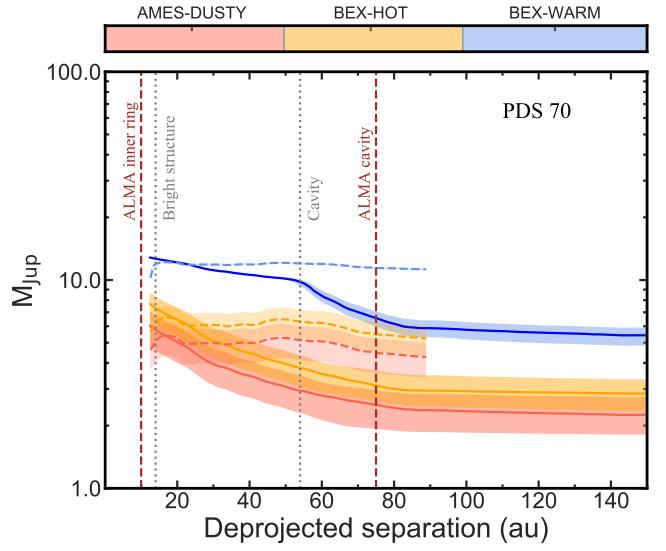
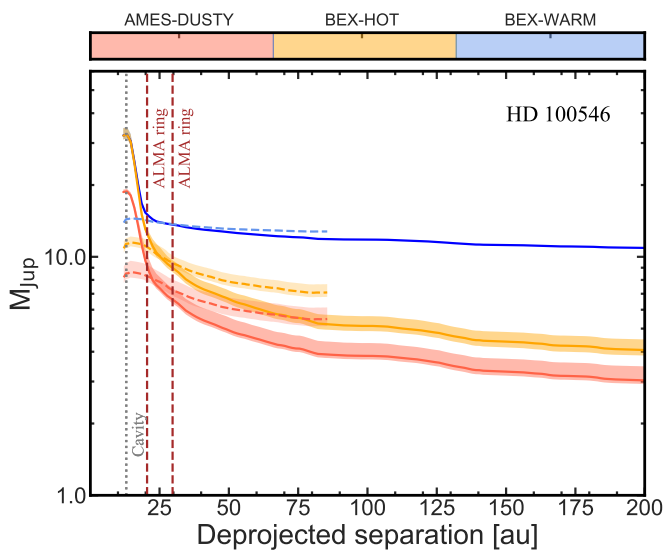**Fig. B.10.** 5σ sensitivity to planet masses in PDS 70 (see Fig. B.1).

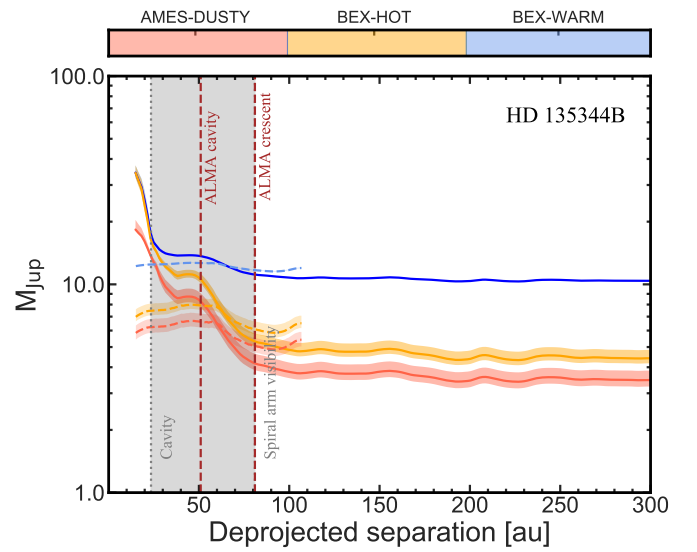**Fig. B.8.** 5σ sensitivity to planet masses in HD 97048 (see Fig. B.1).

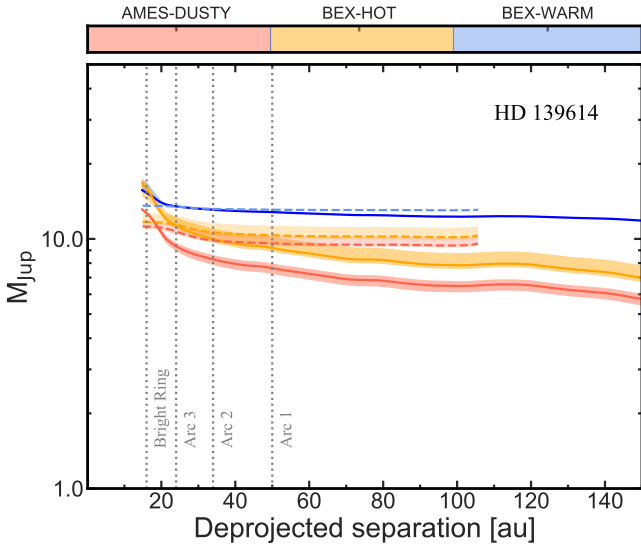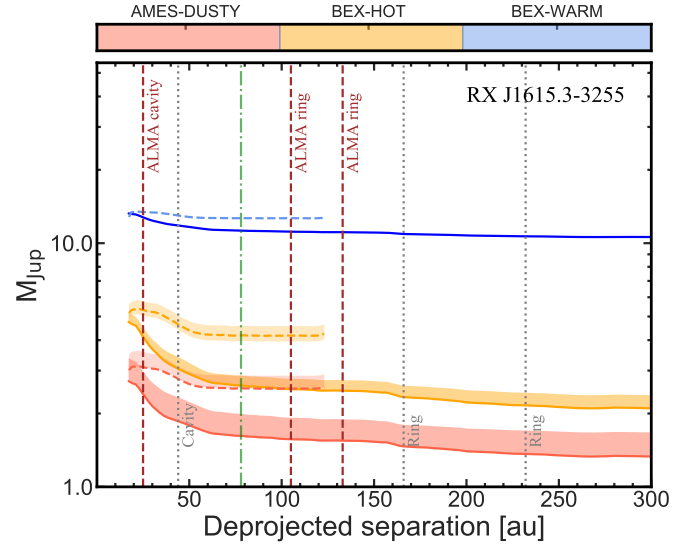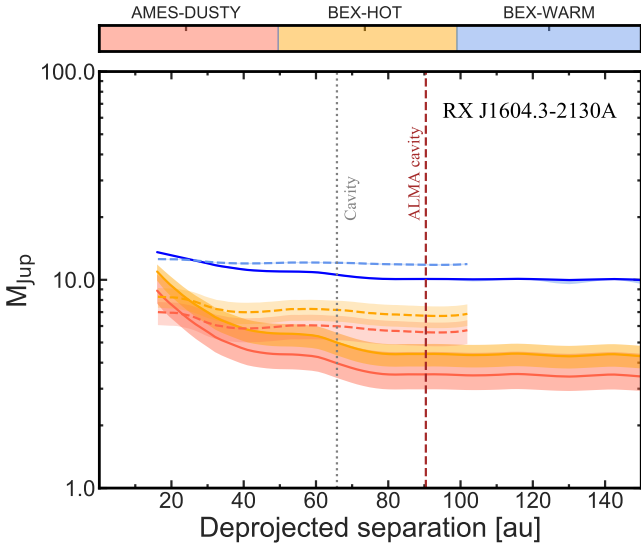**Fig. B.11.** 5σ sensitivity to planet masses in PDS 66 (see Fig. B.2).

Fig. B.12. 5σ sensitivity to planet masses in HD 139614 (see Fig. B.1).

Fig. B.14. 5σ sensitivity to planet masses in RXJ1615 (see Fig. B.1). As the minimum age for this system is below the AMES-DUSTY lower limit, the minimum mass estimate for this model is not included here.

Fig. B.13. 5σ sensitivity to planet masses in RXJ1604 (see Fig. B.1).
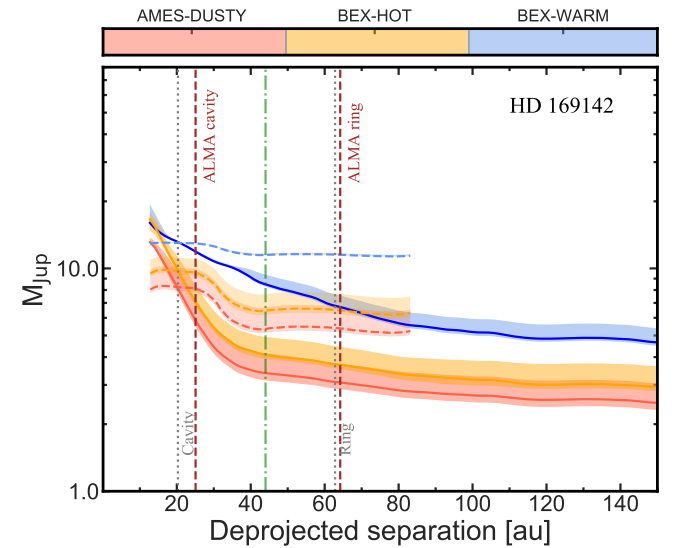
Fig. B.15. 5σ sensitivity to planet masses in HD 169142 (see Fig. B.1).

Appendix C: Detection probability maps

Here we present the detection probability maps to low-mass companions in the PPDs present in our sample (see Table 1). These maps represent the companion mass–semi-major axis parameter space of the SPHERE pupil-tracking data. To obtain them, we first converted the projected 2D limiting magnitude maps from the reduced IRDIFS data to planet masses, using the AMES-DUSTY (Chabrier et al. 2000), BEX-HOT, and BEX-WARM (Marleau et al. 2019a) models. We then ran the MESS code, a Monte Carlo tool for the predictions of exoplanet search results (Bonavita et al. 2012) for each PPD system, which calculates the probability of detecting a planet of a given mass at a given separation. This is achieved by the injection of a set of test companions on different orbits, whose parameters are drawn

from probability distributions. The resulting projected separation of each companion is then calculated and compared to the mass sensitivity of our data at the same location, determining whether or not the planet would have been found by SPHERE. For each target we generated a uniform grid of mass and semi-major axis in the interval [0.5, 200] $M_{\rm Jup}$ and [1, 1000] au with a sampling of 0.5 $M_{\rm Jup}$ and 0.5 au, respectively. We then generated 10^4 orbits for each point in the grid, randomly oriented in space from uniform distributions in ω, e, and M, corresponding to the argument of periastron with respect to the line of nodes, eccentricity, and mean anomaly, respectively, while the inclination and position angles were fixed to be in the disk plane (Table 2).
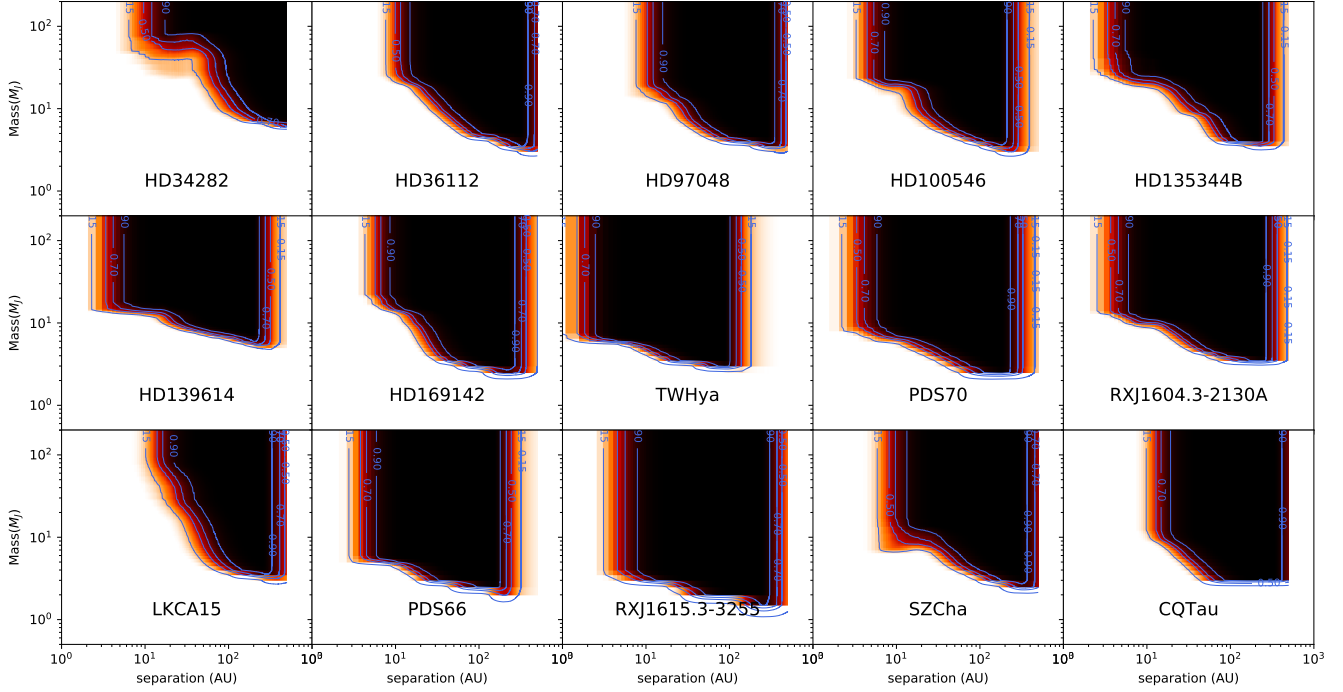
Fig. C.1. SPHERE/IRDIS detection probability maps for the sample of PPD systems considered in this work. The nominal ages of Table 1 and AMES-DUSTY conditions have been assumed to convert ANDROMEDA contrast limits to companion masses. The blue curves circumscribe the probability of detecting a planet of a given mass–semi-major axis space.
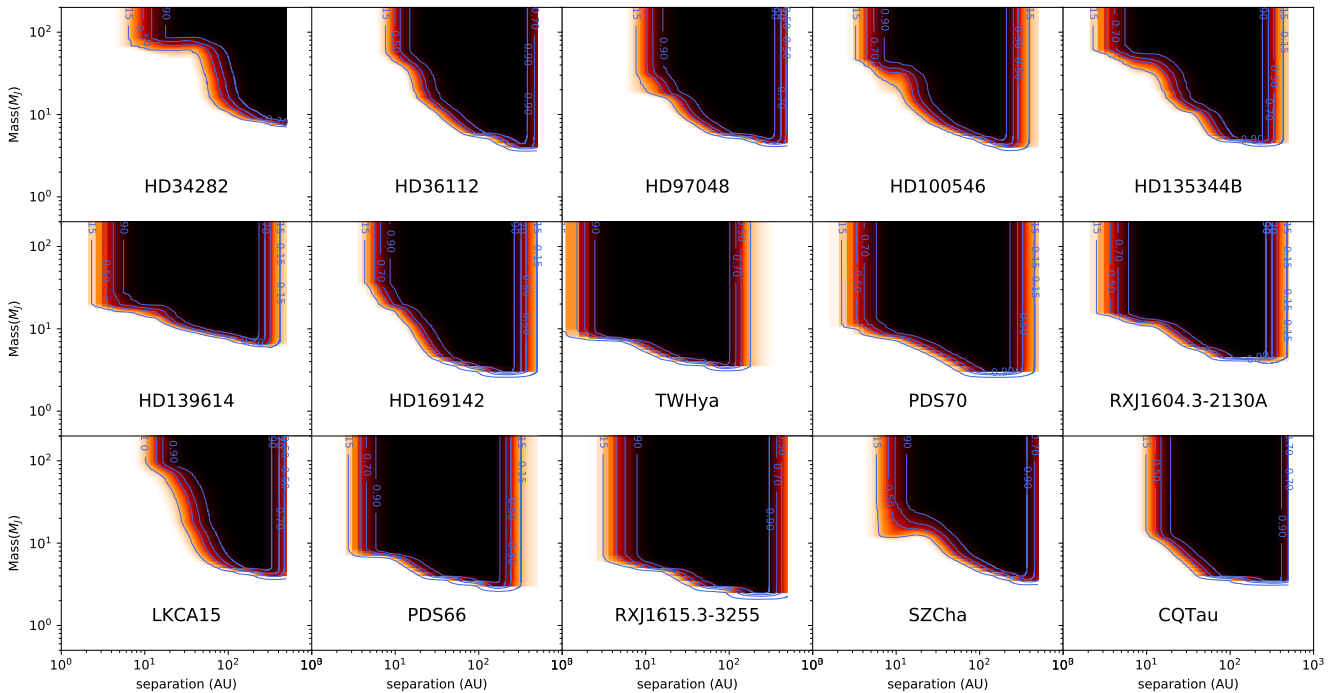

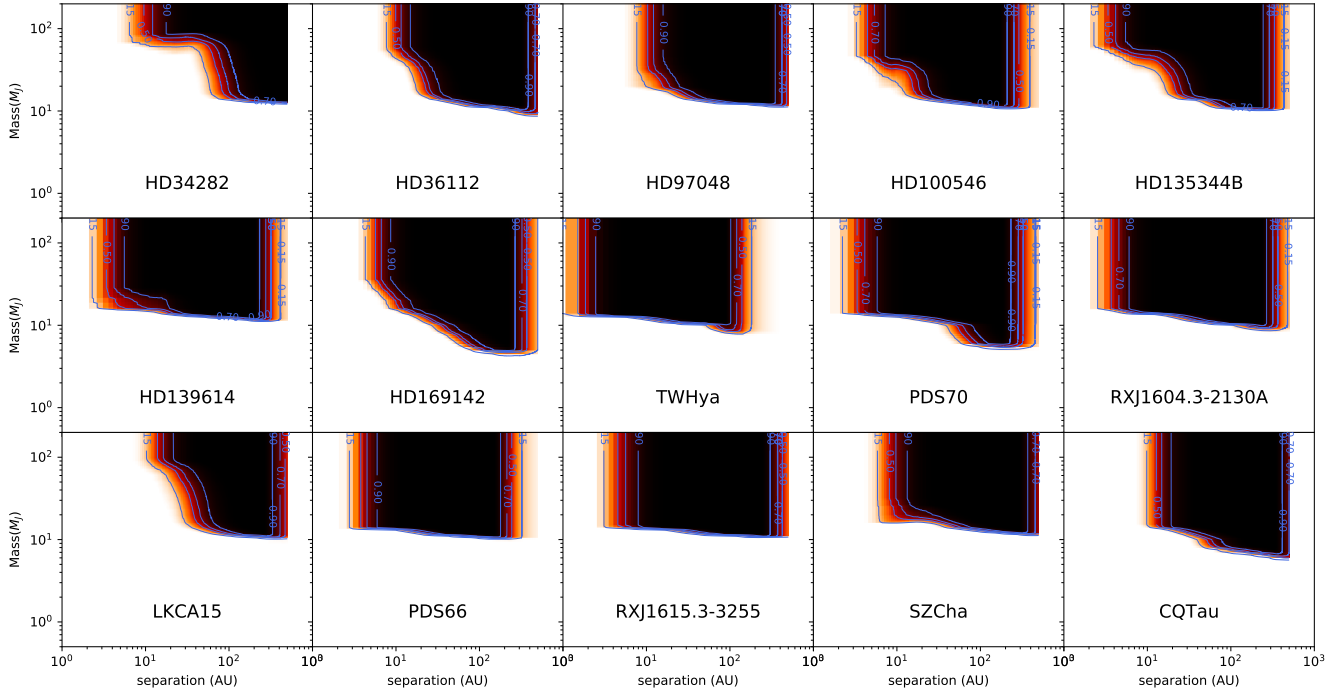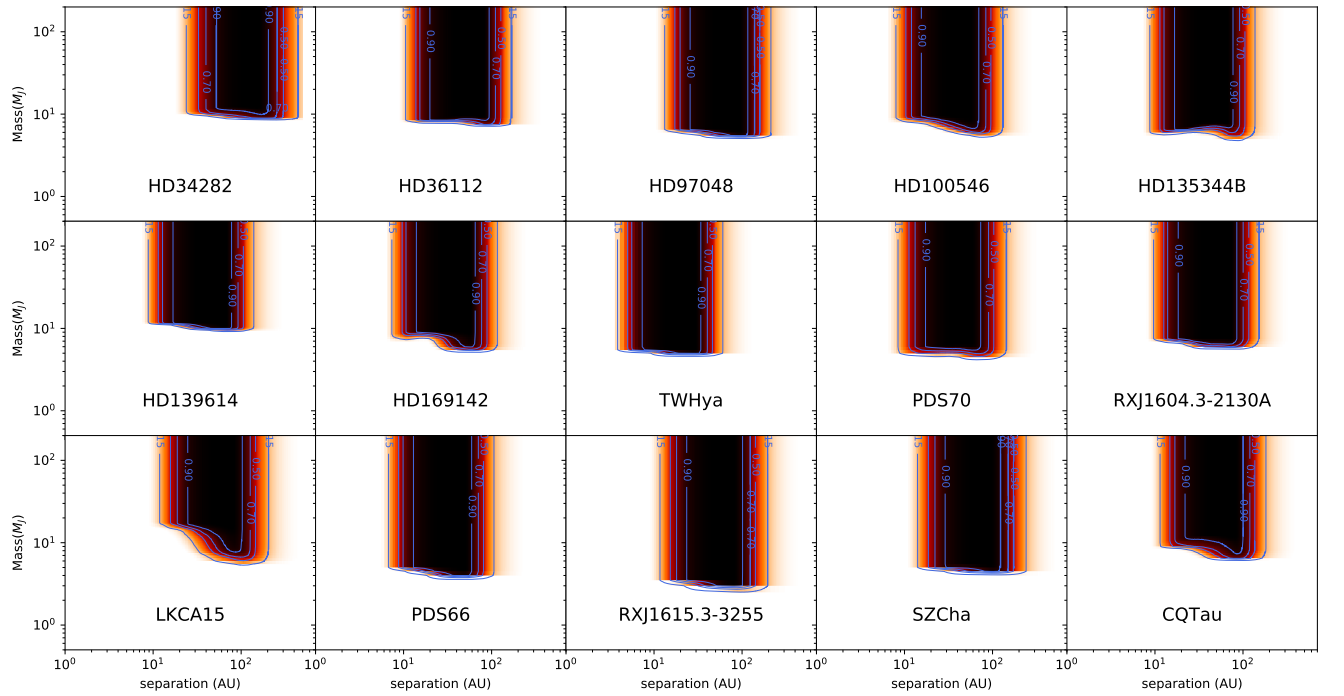**Fig. C.2.** Same as C.1, but for BEX-HOT conditions.

Fig. C.3. Same as C.1, but for BEX-WARM conditions.

Fig. C.4. SPHERE/IFS detection probability maps for the sample of PPD systems considered in this work. The nominal ages of Table 1 and AMES-DUSTY conditions are assumed to convert the ASDI contrast limits to companion masses. The blue curves circumscribe the probability of detecting a planet of a given mass–semi-major axis space.
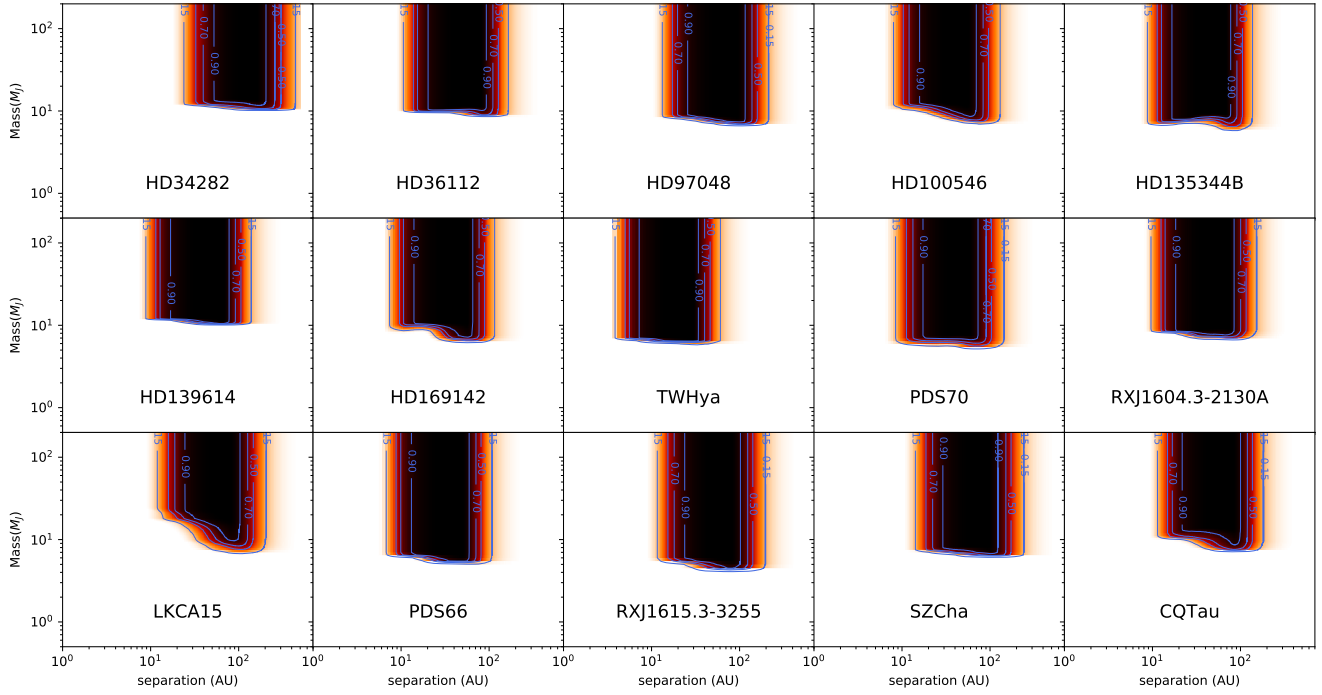
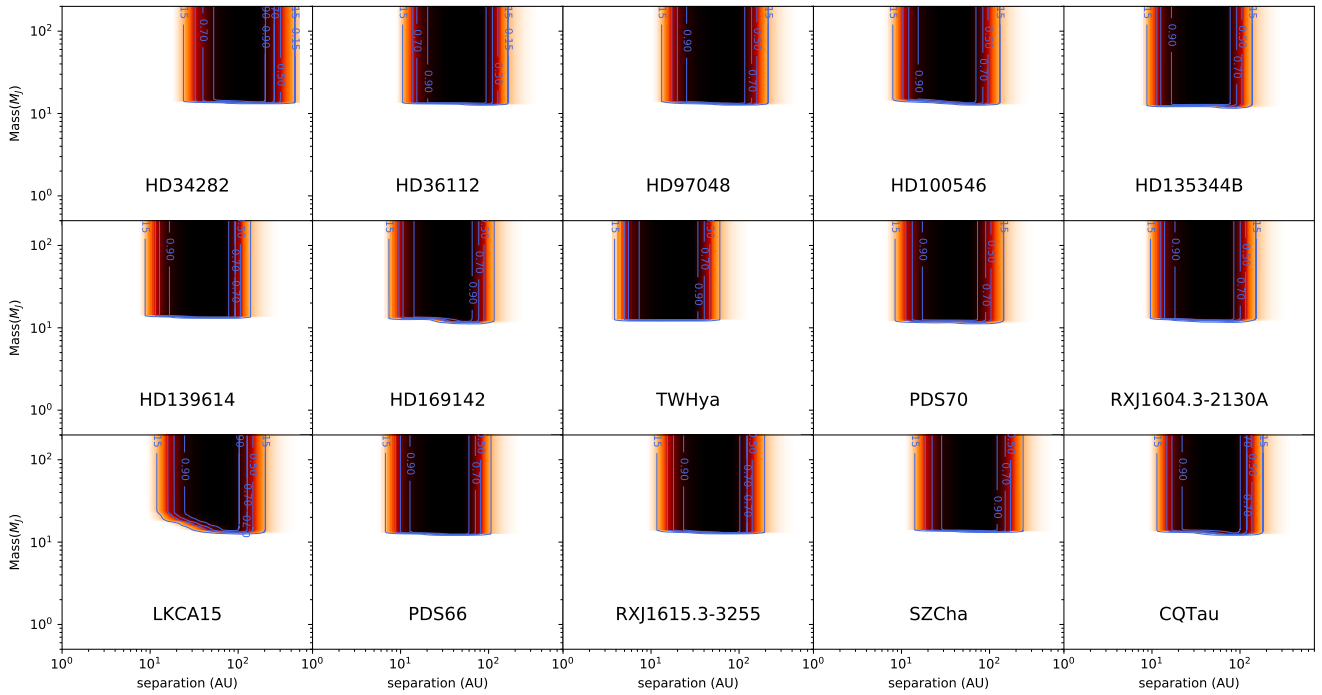**Fig. C.5.** Same as C.4, but for BEX-HOT conditions.

Fig. C.6. Same as C.4, but for BEX-WARM conditions.